https://doi.org/10.5194/egusphere-2026-2061
Preprint. Discussion started: 15 June 2026

Coupling the atmospheric model Meso-NH-v5.5 with the Monte-Carlo solver of conductive-radiative-convective heat exchanges stardis-v0.11.1 to calculate the surface energy balance of complex geometries

Robert Schoetter[1], Cyril Caliot[2], Florent Retailleau[2], Tim Nagel[1], Christophe Coustet[3], Vincent Eymet[3], Vincent Forest[3], Frédéric Hourdin[4], Atsushi Inagaki[5], Simone Kotthaus[6], Valéry Masson[1], William Morrison[7], and Najda Villefranque[1]

[1]Météo-France, CNRS, Univ. Toulouse, CNRM, Toulouse, France
[2]LMAP, CNRS/UPPA, Anglet, France
[3]Méso-Star SAS, Toulouse, France
[4]LMD/CNRS/UPMC, Paris, France
[5]Institute of Science Tokyo, Japan
[6]SIRTA-IPSL, Palaiseau, France
[7]SAGES, University of Edinburgh, United Kingdom

Correspondence: Robert Schoetter (robert.schoetter@meteo.fr)

Abstract. The meteorological impact on humans and infrastructure in urban areas is strongly influenced by the air temperature, humidity, wind velocity, and radiative fluxes. These can be strongly heterogeneous in urban environments with complex 3-D building and vegetation geometry. Micrometeorological building-resolving models have been developed to solve the prognostic equations of the atmospheric variables in urban areas at metric resolution. They take into account the radiative exchanges in the 3-D urban geometry and heat conduction in the building and ground surfaces with separate deterministic approaches. An alternative introduced in this study is to solve the 3-D heat conduction, radiation, and convection with the stochastic Monte-Carlo Method (MCM) in a unified algorithm. Such MCM solvers have become available thanks to recent breakthroughs in the Monte-Carlo community, which allow to establish a connection between conductive and radiative random walks. The advantage of the MCM is that the calculation is independent of the complexity of the urban geometry, the calculations can deal with a large range of scales, and are easy to parallelise. In this study, the coupling between the atmospheric model Meso-NH and the Monte-Carlo solver stardis of conductive-radiative-convective heat exchanges is presented. Humid processes cannot yet be considered with the new model. The coupled model is evaluated against observational data for dry heat wave conditions at the impervious Comprehensive Outdoor Scale MOdel (COSMO) urban-like site in the northern outskirts of Tokyo (Japan). Evaluation results show that the model represents well the temporal evolution of the sensible heat flux and the vertical profiles of air temperature in the urban roughness sublayer. Future developments could focus on including urban vegetation and moist processes such as to enable the study of adaptation measures in urban areas.

https://doi.org/10.5194/egusphere-2026-2061
Preprint. Discussion started: 15 June 2026

1 Introduction

Urban areas alter the local climate due to the different surface energy, water, and momentum balances compared to surrounding rural areas (Oke et al. (2017), Masson et al. (2020)). The nocturnal urban heat island (UHI) can reach 5 to 10 K during favourable meteorological conditions (Oke, 1973). This can influence human thermal comfort and health (Gosling et al. (2009), Gabriel and Endlicher (2011), Forceville et al. (2024)), or building energy consumption for heating and air conditioning (Li et al., 2019). In the context of regional climate change (IPCC, 2022), the UHI can amplify heat stress, morbidity and mortality of city dwellers during more frequent, more intense and longer heat waves. Strategies like urban vegetation (Norton et al. (2015), Gunawardena et al. (2017)), the use of construction materials with higher albedo (Akbari et al., 2012), building renovation (Chatterjee et al., 2025), or electricity production in urban areas (Masson et al., 2014) are promising to contribute to climate change mitigation and adaptation.

Physically-based numerical urban climate models can be used to quantify urban climate processes, the impact of the urban climate on the inhabitants and infrastructure, and the effectiveness of mitigation and adaptation measures. Two main categories of such models exist, the urban canopy models (Lipson et al., 2024) designed for the kilometric and hectometric resolutions and the building-resolving models (Toparlar et al., 2017) designed for the metric resolution.

The urban canopy models like the Town Energy Balance (TEB, Masson (2000)), the Single-Layer Urban Canopy Model (SLUCM, Kusaka et al. (2001)), or the Building Effect Parameterization (BEP, Martilli et al. (2002)) represent the 3-D nature of urban areas, but they strongly simplify the urban morphology, e.g. by assuming an infinitely long street canyon. The simplified morphology conserves district average parameters like the plan area building density (λ_p), the external facade density (λ_w), and the average building height (H_{mean}) such as to capture the bulk of the urban influence on the atmosphere. Urban canopy models have proven successful in simulating the urban energy balance (Grimmond et al., 2010), they have been coupled to mesoscale atmospheric models to analyse urban climate processes (Lemonsu and Masson, 2002), to numerical weather prediction models like TEB in the operational AROME-France (Seity et al., 2011), and to regional climate models (Lemonsu et al., 2023).

The building-resolving models like ENVI-Met (Bruse and Fleer, 1998), IBM-WRF (Lundquist et al., 2012), SOLENE-microclimate (Morille et al., 2015), PALM-4U (Maronga et al., 2020), uDALES (Suter et al., 2022), or City-LES (Kusaka et al., 2024) resolve the buildings explicitly. This can be done by employing a body-fitted grid or Immersed Boundaries (Moonen et al., 2012), or a body-force method that consists of applying a strong drag force at the location of the buildings (Muñoz-Esparza et al., 2020). The building-resolving models can simulate meteorological variables like mean wind velocity, turbulence, radiation, or pollutant concentrations that are strongly heterogeneous in the complex 3-D building and vegetation geometry. They can be employed to quantify the impact of adaptation measures at the scale of individual buildings or to quantify uncertain parameters like the momentum drag coefficient due to buildings that are used by the urban canopy models (Nagel et al., 2023). The building-resolving models need to operate at metric resolution and employ a low time step leading to very high computational cost. This prohibits their application in numerical weather prediction or regional climate models.

The urban climate models need to represent the solar and terrestrial radiation exchanges in the urban canopy layer and the

https://doi.org/10.5194/egusphere-2026-2061
Preprint. Discussion started: 15 June 2026

heat conduction in the building and ground materials to accurately simulate the urban energy balance. The radiosity method is frequently used for the calculation of the 3-D radiation exchanges (Schoetter et al., 2023). With the radiosity method, the building and the ground are divided into N_f facets, and exchange factors between the facets are calculated. These exchange factors quantify which fraction of the radiative flux starting at facet i ($1 \leq i \leq N_f$) is reaching facet j ($1 \leq j \leq N_f$). Assuming a constant irradiation of each facet, broadband albedo and emissivity, isotropic reflection and emission, and vacuum in the urban canopy layer, it is possible to calculate the solar and terrestrial radiation reveiced by each facet (Krayenhoff et al., 2014). The drawback of the radiosity method in the building-resolving models is that a large number of exchange factors needs to be calculated and stored in memory. Also physical processes like direct solar irradiation, specular reflections, or interaction of radiation with air, aerosols, or clouds in the urban canopy layer cannot be represented. Krč et al. (2021) introduced an angular discretisation that divides the view from each facet into a fixed number of directions and was able to improve the scaling of the number of exchange factors with the size of the domain in PALM-4U. However, this introduces additional model assumptions and uncertainties.

The urban climate models calculate the heat conduction in the buildings and the ground materials independently of radiative transfer and in 1-D. This assumes purely 1-D heat conduction and homogeneous wall materials (e.g. Yang and Li (2013) for ENVI-MET 4.0, Pfafferott et al. (2021) for PALM-4U, Kusaka et al. (2024) for City-LES), which makes it difficult to represent features like thermal bridges in walls, or roofs with a complex shape. Building energy models have been developed for the urban canopy models (Kikegawa et al. (2003), Salamanca et al. (2009), and Bueno et al. (2012)) to solve the energy budget of a representative building at district scale. For the building-resolving urban climate models, Pfafferott et al. (2021) coupled a building energy model that is based on a resistance network to PALM-4U whereas Suter et al. (2022) impose a Dirichlet boundary condition of constant indoor air temperature in uDALES.

An alternative to the established deterministic approches for the calculation of the conductive-radiative-convective heat exchanges between a complex 3-D urban geometry and the atmosphere is to use the stochastic Monte-Carlo Method (MCM). The MCM is well established to solve the Radiative Transfer Equation and has been successfully employed to calculate urban radiative exchange (Caliot et al., 2023). A recent advancement in resolving conductive heat transfer using the MCM establishes a connection between conductive and radiative random walks at the Robin boundary condition. This is achieved through probabilisation and a double randomisation technique, enabling the construction of a unified path that explores the domain to trace known sources backward in time (Villefranque et al. (2022), Tregan et al. (2023)). The heat conduction equation in the solid (like the building or ground materials) with Robin boundary conditions can be coupled to the Radiative Transfer Equation in the transparent fluid medium (like the atmosphere) (Caliot et al., 2024). Convective heat exchange at the solid-fluid interface (e.g. the sensible heat flux from buildings to the atmosphere) can also be taken into account. This is promising since it allows to solve 3-D radiative transfer and 3-D heat conduction in the complex urban geometry with one unified algorithm and a high degree of physical realism. To determine the wall temperature, the MCM incorporates the convective heat flux at the boundary, as defined by Newton's law of cooling. This law involves a known heat transfer coefficient and the fluid temperature. The convective heat flux at the boundary is further influenced by the fluid flow near the boundary, which can be resolved using a computational fluid dynamics (CFD) solver. The use of the MCM has the advantages that 1.) the computational time to solve

https://doi.org/10.5194/egusphere-2026-2061
Preprint. Discussion started: 15 June 2026

the conductive-radiative-convective paths with the MCM does not depend on the complexity of the geometry (Villefranque et al., 2022), 2.) the calculations allow to deal with large ranges of scales in the scene, i.e. the so-called *teapot in a stadium problem* has been solved by the Monte-Carlo (MC) community, and 3.) the calculations are easy to parallelise.

The objective of this study is to present the coupling of the atmospheric model Meso-NH (Lac et al., 2018) that contains an Immersed Boundary Method (IBM) to represent buildings or orography (Auguste et al., 2019, 2020) with the stardis Monte-Carlo solver of conductive-radiative-convective heat exchanges to solve the energy budget of a complex urban geometry. The initial version of the coupled model cannot deal with moist processes and is therefore evaluated for dry and sunny conditions at the impervious Comprehensive Outdoor Scale MOdel (COSMO, Kanda et al. (2007)) urban-like site in the outskirts of Tokyo (Japan). The coupling is presented in Sect. 2, the setup for the evaluation in Sect. 3, the results in Sect. 4. A discussion is made in Sect. 5, and conclusions are drawn in Sect. 6.

2 Coupling between Meso-NH and stardis

The main idea of the coupling (Figs. 1 to 3) is that Meso-NH-IBM is used to solve the prognostic equations in the atmosphere and writes meteorological forcing data required by stardis to disc. Stardis calculates the surface temperature of the ground and immersed obstacles with a backward MC algorithm and accesses the meteorological forcing data that Meso-NH-IBM has written since the beginning of the simulation.

https://doi.org/10.5194/egusphere-2026-2061
Preprint. Discussion started: 15 June 2026

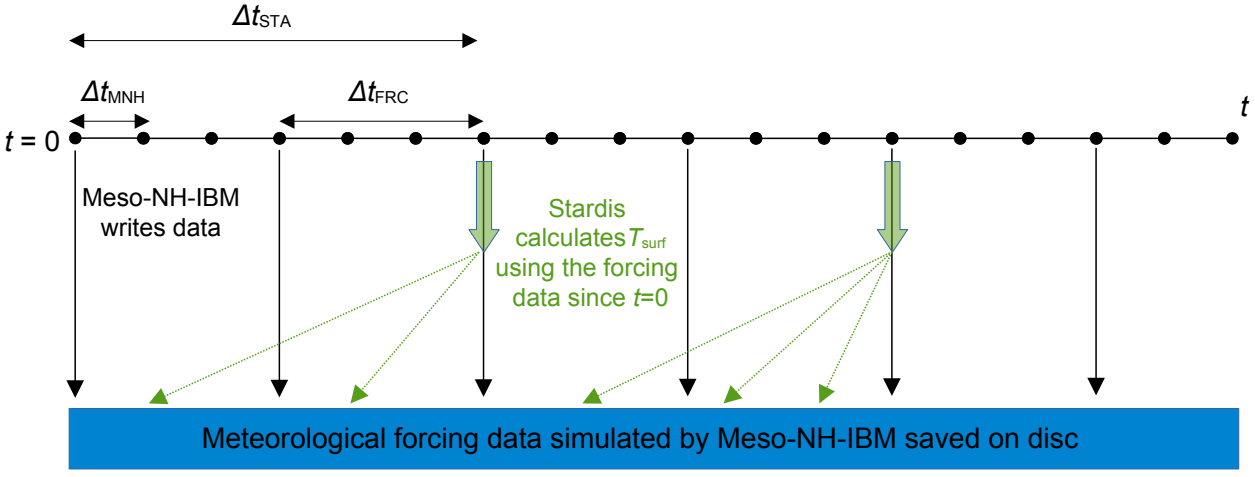

Figure 1. Temporal execution of the coupled Meso-NH-IBM-stardis with the time step of Meso-NH-IBM (Δt_{MNH}) used to solve the prognostic atmospheric equations, the time step for writing the forcing data (Δt_{FRC}) and the time step for calculation of surface temperature with stardis (T_{surf}) (Δt_{STA}).

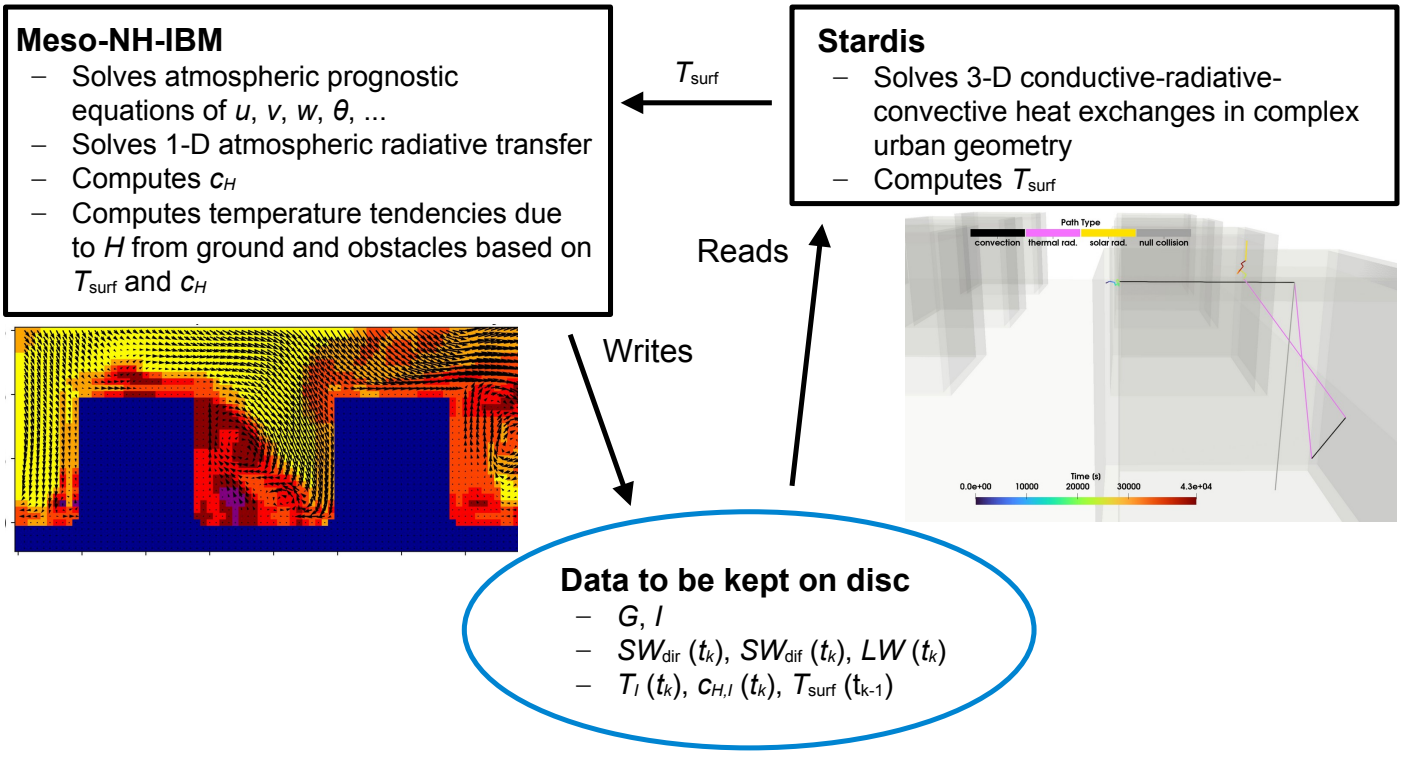

Figure 2. Data transfer between Meso-NH-IBM, stardis, and the disc. The data that need to be stored on disc are the positions of the ghost (G) and image points (I), the time series of downwelling direct solar (SW_{dir}), diffuse solar (SW_{dif}), and terrestrial infrared radiation LW as well as air temperature (T), exchange coefficient for sensible heat (c_H), and surface temperature (T_{surf}) at the image points (I). t_k is the time at which the forcing data are written.

https://doi.org/10.5194/egusphere-2026-2061
Preprint. Discussion started: 15 June 2026

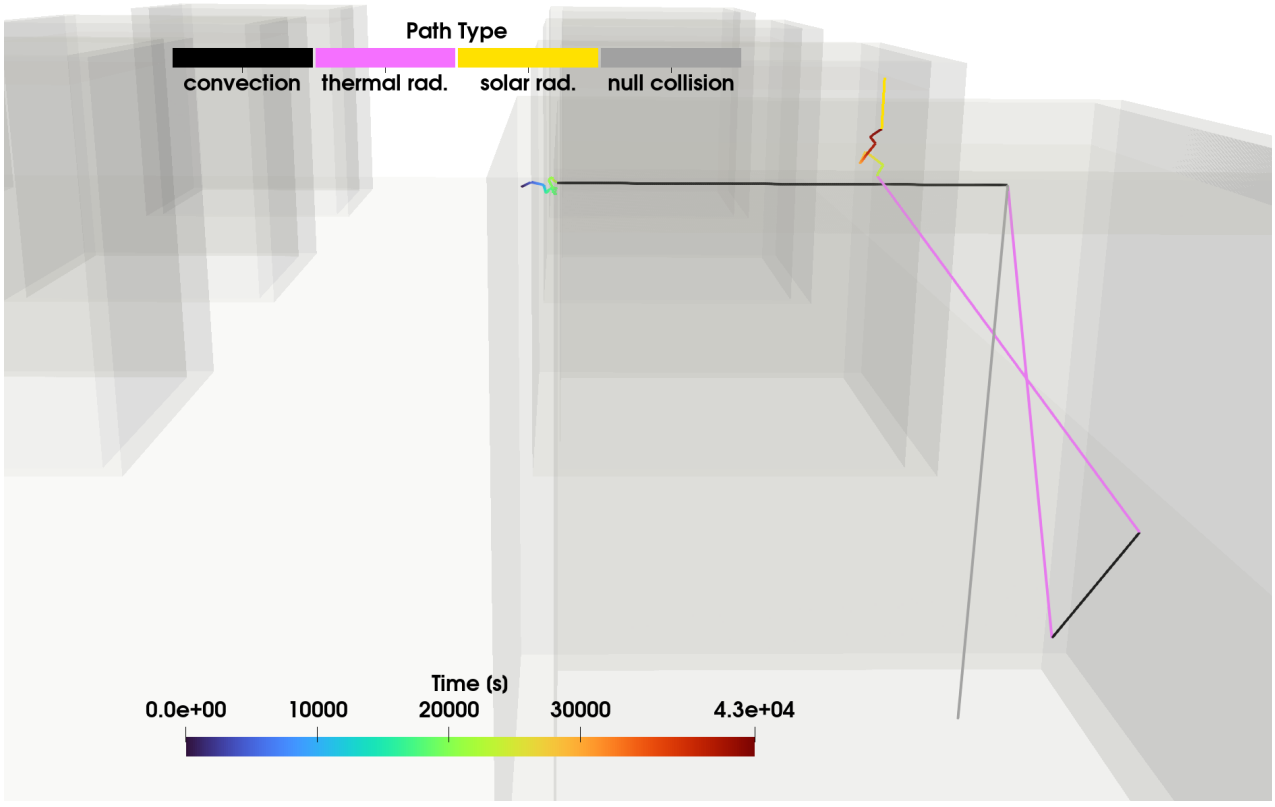

Figure 3. Example of a conductive-radiative-convective path that starts at $t = 43200$ s on the top of a cube at the interface between the cube and the air. It receives direct radiation from the sun, then travels via heat conduction through the cube top solid to reach the interface between the cube top solid and the internal air at $t \approx 26000$ s. It further travels instantaneously via thermal radiation and convection in the cube internal cavity. For the convection in the internal cavity, it is assumed that the fluid is perfectly stirred. At the interface between a solid and the outdoor air, the path would end in the case a convective path is chosen; the convective heat flux is then taken into account in Meso-NH. The path finally travels from $t \approx 26000$ s to $t = 0$ s via heat conduction through the cube wall. At $t = 0$ s, the conductive path ends inside the cube wall, and the cube wall material initial temperature is reached.

2.1 Atmospheric model Meso-NH with Immersed Boundaries

Meso-NH (Lac et al., 2018) is a mesoscale non-hydrostatic anelastic atmospheric research model. The prognostic equations are based on the conservation of momentum, mass, energy, and humidity. The prognostic variables are the three velocity components (u, v, w; recurrent symbols are given in Appendix C), the potential temperature (θ), the subgrid turbulence kinetic energy (e), and the mixing ratios of water vapour, hydrometeors, passive and reactive scalars. The discretisation is made following a staggered Arakawa C grid and the coordinates follow the terrain. The turbulence scheme is based on a prognostic equation for e, a mixing length closure, and a dissipation proportional to e.

Auguste et al. (2019) introduced an Immersed Boundary Method (IBM) into Meso-NH (Meso-NH-IBM) to allow for the

https://doi.org/10.5194/egusphere-2026-2061
Preprint. Discussion started: 15 June 2026

representation of immersed obstacles, vertical walls, or steep orography that cannot be simulated using terrain-following coordinates. With the IBM, the model domain is split into the fluid region in which the prognostic equations are solved and the solid region. Meso-NH-IBM employs a discrete forcing approach and represents the solid-fluid interface by a level-set function (ϕ). $|\phi|$ is the distance to the solid-fluid interface. $\phi > 0$ denotes areas in the solid region and $\phi < 0$ areas in the fluid region. A ghost-cell technique (GCT) is employed that prescribes values for the prognostic variables at ghost cells inside the solid region such that a desired boundary condition at the solid-fluid interface is imposed. This could for example be a no-slip condition at the solid surface for the velocity tangential to the solid (homogeneous Dirichlet condition) or a zero sensible heat flux at the solid surface (homogeneous Neumann condition). Meso-NH-IBM is only compatible with Cartesian grids, thus any orography has to be represented as an Immersed Boundary. The vector normal to the interface ($\boldsymbol{n}$) can be calculated based on ϕ following

$$\boldsymbol{n} = \frac{\boldsymbol{\nabla}\phi}{|\boldsymbol{\nabla}\phi|} \tag{1}$$

For each ghost point ($G(x_G, y_G, z_G)$) with $\phi = \phi_G$, n layers of image points (I_n) in the fluid region are defined such that their distance to the interface is proportional to the grid spacing (Δ). The vector from G to I_n ($\boldsymbol{GI_n}$) is given by

$$\boldsymbol{GI_n} = \boldsymbol{n}(\Phi_G + n\Delta) \;\text{ for }\; n \in \{0.5, 1, 2\} \tag{2}$$

with

$$\Delta = (\Delta_x \Delta_y \Delta_z)^{\frac{1}{3}} \tag{3}$$

where Δ_x, Δ_y, and Δ_z are the grid sizes in $x-$, $y-$, and $z-$ direction, respectively. With the current Meso-NH-IBM implementation, the grid sizes in all directions have to be equal in the region with immersed obstacles ($\Delta_x = \Delta_y = \Delta_z = \Delta$)
Since the I_n do not coincide with Meso-NH grid points, the prognostic variables (Ψ) need to be interpolated from the Meso-NH grid to the image points (Ψ_{I_n}). Dirichlet ($\Psi_{\phi=0}$) or Neumann boundary conditions ($\Delta \frac{\partial \Psi}{\partial \boldsymbol{n}}|_{\phi=0}$) can be specified at the solid-fluid interface. The value of the prognostic variable at the interface ($\Psi(\phi = 0)$) can be written as a Robin boundary condition:

$$\Psi(\phi = 0) = k_R \Psi_{\phi=0} + (1 - k_R)\left(\Psi(\phi = -n\Delta) - n\Delta \frac{\partial \Psi}{\partial \boldsymbol{n}}\bigg|_{\phi=0}\right) \tag{4}$$

with $k_R = 1$ for a Dirichlet boundary condition and $k_R = 0$ for a Neumann boundary condition. The value of the prognostic variable at the ghost point can be specified following

$$\Psi_G = 2\Psi_{\phi=0} - \Psi_I \qquad \text{for a Dirichlet boundary condition} \tag{5}$$

$$\Psi_G = 2\Phi \frac{\partial \Psi}{\partial \boldsymbol{n}}\bigg|_{\phi=0} + \Psi_I \quad \text{for a Neumann boundary condition} \tag{6}$$

In the following it is described how the conductive, radiative, and convective heat exchanges in a complex 3-D urban geometry are solved to calculate the surface temperature of the ground and immersed obstacles as well as the sensible heat flux.

https://doi.org/10.5194/egusphere-2026-2061
Preprint. Discussion started: 15 June 2026

2.2 Stardis Monte-Carlo solver of conductive-radiative-convective heat exchanges

Stardis (Villefranque et al. (2022), Tregan et al. (2023), Caliot et al. (2024), Caliot et al. (2026)) is employed in *probe computation* mode to calculate the surface temperature (T_{surf}) of the ground and immersed obstacles (e.g. buildings) at probes located at the solid-fluid interface and for a given time of interest (t). For each first layer image point (I_1) in Meso-NH-IBM, the closest point on the solid-fluid interface is defined as the probe point corresponding to I_1. As described in Caliot et al. (2026), mixed conductive, radiative, and convective Monte-Carlo random paths are calculated backwards in time, starting at the probe points, until a known initial or boundary condition is reached (Fig. 3). These boundary conditions are:

- For conductive heat transfer, the temperature in the deep soil (e.g. in 10 m depth) is prescribed as a Dirichlet boundary condition. Furthermore, initial values ($t = 0$) of the temperatures of the solids (e.g. building walls, roofs, the ground) and internal fluids (e.g. building indoor air temperature) are prescribed.
- For radiative heat transfer, the boundary conditions are the time series since the beginning of the simulation ($t = 0$) of downwelling direct solar, diffuse solar, and terrestrial infrared radiative flux density at the top of the urban canopy layer.
- For convective heat transfer, the time series, since the beginning of the simulation, of sensible heat flux H_{I_1} between the solid and the atmosphere is prescribed.

Given that the MC random paths are calculated backwards in time, the meteorological forcing data required for the calculation of the sensible and radiative heat exchanges between the immersed obstacles and the atmosphere need to be stored on disc or in memory (Fig. 1 and Fig. 2). In order to reduce the computational cost, temporal averages of the meteorological forcing data instead of instantaneous values are stored. Furthermore, the solid surface temperature is calculated with stardis not for each time step of Meso-NH-IBM, but for a larger conductive-radiative-convective time step. This choice is justified for two main reasons:

- Obstacle-resolving simulations with Meso-NH-IBM are carried out in Large-Eddy Simulation (LES) mode at a very low time step (0.01 s to 1 s). Therefore, the meteorological forcing close to the immersed obstacles (e.g. u, θ) exhibits high-frequency turbulent fluctuations (Fig. 2). It is assumed that it is not necessary to store these high-frequency fluctuations during a building-resolving simulation of several hours or days. For example, assuming that the surface temperature of a building wall shall be computed at $t = 129600$ s (at noon on the second day of the simulation), this result will not be influenced in a relevant manner by the turbulent θ fluctuations close to the building or ground surfaces during the first day of the simulation (e.g. at $t = 57600$ s). The result will however depend on the average values of θ during the first day of the simulation since they will influence the sensible heat exchange between the buildings and the atmosphere.
- Stardis is not used at each time step of Meso-NH-IBM to update the surface temperatures, since for applications to urban climate, these surface temperatures are unlikely to change very rapidly. This might lead to uncertainties for some types

https://doi.org/10.5194/egusphere-2026-2061
Preprint. Discussion started: 15 June 2026

of surfaces (e.g. windows or vegetation leaves) for meteorological situations with rapidly changing solar irradiation (e.g. cumulus clouds). In such cases, the time step for the conductive-radiative-convective exchanges could be reduced.

Under these assumptions, three different time steps (Fig. 1) are defined for coupled Meso-NH-IBM-stardis simulations:

- Δt_{MNH} is the time step used by Meso-NH-IBM to solve the prognostic equations of the atmospheric variables. It is mainly governed by the wind speed and the grid size.
- Δt_{FRC} is the time step for writing the meteorological forcing required by stardis that are calculated based on the Meso-NH-IBM prognostic variables. The meteorological forcing data are thus written every $t_k = k\ \Delta t_{\mathrm{FRC}}, k\ \in\ [0..N_{\max}]$. $N_{\max}$ is the maximum number of forcing time steps depending on the required simulation duration.
- Δt_{STA} is the time step for the calculation of T_{surf} at the probe points with stardis.

For the simplification of the technical implementation, Δt_{FRC} must be a multiple of Δt_{MNH}, and Δt_{STA} a multiple of Δt_{FRC}. The meteorological forcing data for stardis are averaged over N_{FRC} Meso-NH-IBM time steps with

$$N_{\mathrm{FRC}} = \frac{\Delta t_{\mathrm{FRC}}}{\Delta t_{\mathrm{MNH}}} \tag{7}$$

Stardis also computes the standard deviation of T_{surf} (σ_T) at each probe point such as to quantify the uncertainty of the MC based calculation. The MC algorithm shows a good convergence if σ_T is proportional to $\frac{1}{\sqrt{N}}$, with N the number of realisations of the MC algorithm.

2.3 Meteorological forcing for stardis calculated by Meso-NH-IBM

For each t_k, Meso-NH-IBM writes the following data required by stardis to disc.

- The calendar day (year, month, day) and time (in UTC) corresponding to this forcing time t_k.
- The solar zenith and azimuth angle.
- The domain-averaged downwelling direct solar, diffuse solar, and terrestrial infrared radiation at the top of the urban canopy layer.
- The air temperature at the image points.
- The exchange coefficient for the sensible heat flux at the image points.
- The skin surface temperature simulated by stardis for the previous conductive-radiative-convective time step ($T_{\mathrm{surf}}(t - \Delta t_{\mathrm{STA}})$).

The choice has been made to write $T_{\mathrm{surf}}(t-\Delta t_{\mathrm{STA}})$ to disc to be used as reference temperature (T_{ref}) for the linearised infrared radiative exchanges. Assuming a surface with broadband emissivity ($\epsilon = 1$) and surface temperature T_{surf}, the emitted radiation is given by

$$LW_{\mathrm{emit}} = \sigma {T_{\mathrm{surf}}}^4 = 4\ \sigma {T_{\mathrm{surf}}}^4 - 3\ \sigma T_{\mathrm{surf}}^4 \tag{8}$$

https://doi.org/10.5194/egusphere-2026-2061
Preprint. Discussion started: 15 June 2026

Due to the difficulty of the MCMs to deal with non-linearities, a linearisation of the infrared radiative exchanges around a reference temperature ($T_{\mathrm{ref}} \approx T_{\mathrm{surf}}$) is made. In the case T_{ref} is not too different from T_{surf}, Eq. 8 can be written as:

$$LW_{\mathrm{emit}} \approx 4\,\sigma {T_{\mathrm{ref}}}^3 (T_{\mathrm{surf}} - \frac{3}{4} T_{\mathrm{ref}}) \tag{9}$$

For applications to urban microclimate modelling, the specification of a constant, uniform value of T_{ref} can lead to too large deviations of this approximation from the real solution. This is because the solar irradiation can heat urban surfaces to 60 to 70° while they exchange infrared radiation with shaded surfaces that could be at 20 to 30° or the sky that could be even cooler. For this reason, the T_{surf} values simulated at the last condutive-radiative-convective time step ($t - \Delta t_{\mathrm{STA}}$) are saved to disc and used as T_{ref}:

$$T_{\mathrm{ref}}(t) = T_{\mathrm{surf}}(t - \Delta t_{\mathrm{STA}}) \tag{10}$$

Domain-averaged values (indicated by the $<>$ in the equations) of downwelling direct solar ($< SW_{\mathrm{dir}} >$), diffuse solar ($< SW_{\mathrm{dif}} >$), and terrestrial infrared ($< LW >$) radiation above the urban canopy layer are used as top radiative boundary conditions for stardis. They can be taken from the atmospheric model's radiation scheme or from observations.

For each t_k, the downwelling radiation is time averaged (indicated by the overline) over the period from $t - \Delta t_{FRC} + \Delta t_{\mathrm{MNH}}$ to t:

$$\overline{< SW_{\mathrm{dir}} >} = \frac{1}{N_{\mathrm{FRC}}} \sum_{i=0}^{N_{\mathrm{FRC}}-1} < SW_{\mathrm{dir}}(t - i\,\Delta t_{\mathrm{MNH}}) > \tag{11}$$

$$\overline{< SW_{\mathrm{dif}} >} = \frac{1}{N_{\mathrm{FRC}}} \sum_{i=0}^{N_{\mathrm{FRC}}-1} < SW_{\mathrm{dif}}(t - i\,\Delta t_{\mathrm{MNH}}) > \tag{12}$$

$$\overline{< LW >} = \frac{1}{N_{\mathrm{FRC}}} \sum_{i=0}^{N_{\mathrm{FRC}}-1} < LW(t - i\,\Delta t_{\mathrm{MNH}}) > \tag{13}$$

For each t_k, time averages of air temperature ($\overline{T}$), exchange coefficient for sensible heat ($\overline{c_H}$), and the surface temperature simulated by stardis for the previous conductive-radiative-convective time step ($\overline{T_{\mathrm{surf}}}(t - \Delta t_{\mathrm{STA}})$) at the image points of the first layer (I_1) are written to the disc.

$\overline{T_{I_1}}$ is calculated following

$$\overline{T_{I_1}} = \frac{1}{N_{\mathrm{FRC}}} \sum_{i=0}^{N_{\mathrm{FRC}}-1} \Theta_{I_1}(t - i\,\Delta t_{\mathrm{MNH}})\,\Pi_{I_1}(t - i\Delta t_{\mathrm{MNH}}) \tag{14}$$

The Exner function (Π) is given by

$$\Pi = \left(\frac{p}{P_{r0}}\right)^{\frac{R_d}{c_p}} \tag{15}$$

with p the local pressure, P_{r0} the ground level pressure of the reference state, R_d the gas constant of dry air, and c_p the specific heat capacity at constant pressure of dry air. The calculation of the exchange coefficient is given in Appendix A.

https://doi.org/10.5194/egusphere-2026-2061
Preprint. Discussion started: 15 June 2026

2.4 Calculation of the sensible heat flux in Meso-NH-IBM

The sensible heat flux at the immersed obstacles for a given image point ($\overline{H_{I_1}}$) is calculated in Meso-NH-IBM following

$$\overline{H_{I,1}} = \overline{c_{H_{I,1}}} \left(\frac{\overline{T_{\mathrm{surf},I_1}}}{\overline{\Pi_{I_1}}} - \overline{\theta_{I_1}} \right) \tag{16}$$

A verification of energy conservation has been implemented to test whether the increment of θ due to the IBM in Meso-NH is consistent with the energy exchanged with the surface.

2.5 Current limitations and potential future improvements

The coupling between Meso-NH-IBM and stardis introduced here is only a first step and some of the most important limitations are mentioned as follows.

- A point value (at the probe point positions) of the solid surface temperature is calculated by stardis. To increase the precision, stardis could be adapted to calculate an average surface temperature for all solid-fluid interfaces located in the corresponding Meso-NH-IBM grid point.
- Time-averaged meteorological forcing data are used by stardis. This filters high frequency turbulent fluctuations, which are assumed to not have a large influence on the probe temperatures. However, the results might depend on the selected time step for writing the forcing data. A different time step might be appropriate for different applications.
- The meteorological forcing data that is accessed by stardis during the backward random conductive-radiative-convective paths is located at the image point positions and only available for discrete time intervals. The random paths however can reach any given point on the solid-fluid interface at any given time between the current time and the beginning of the simulation. The choice has been made to use the closest forcing point and to interpolate linearly in time. Both choices can introduce uncertainties.
- In stardis, the downwelling radiative flux densities at the top of the urban canopy layer do not depend on the position. This approximation is useful for the simulation of a small domain like a district of a city, but it could not be applied for domains larger than a few km. Furthermore, both the downwelling terrestrial radiation and the diffuse solar radiation are assumed to be isotropic.
- The surface temperature is updated with a larger time step than the one used by the atmospheric model. This choice will be good in most situations, but there could be cases with strong variation of solar irradiation (e.g. cumulus clouds) for which this simplification is not valid.
- The backward conductive-radiative-convective paths can reach areas outside of the domain of the atmospheric model. Therefore, the domain (e.g. the urban geometry) used by stardis must be larger than the one used by the atmospheric model. Depending on the application case, appropriate strategies must be developed on how to extrapolate the meteorological forcing data to the areas outside of the atmospheric model domain. This uncertainty must be nuanced, since for

https://doi.org/10.5194/egusphere-2026-2061
Preprint. Discussion started: 15 June 2026

an application to a real geometry, the building-resolving atmospheric model results could also be strongly influenced by not well represented buildings outside of the model domain.

- Scattering and absorption of radiation in the urban canopy layer by the air, aerosols, or fog is not considered in the current version of stardis. This could be an issue, especially for terrestrial radiation (Hogan (2019), Schoetter et al. (2023)).

- The indoor air is assumed to be perfectly stirred. The indoor air temperature evolves freely as a function of the conductive and radiative heat fluxes through the building envelope. The value of c_H for convection between the indoor surfaces and the indoor air is set to a fixed value. The same is made for the thermal infrared emissivity (ϵ) of internal surfaces, and the reference temperature for indoor infrared radiative exchanges.

- No exchanges of air between the building indoor and the atmosphere are taken into account. These could be via infiltration through small holes in the building envelope, natural or mechanical ventilation. Such processes could be taken into account by a modification of the MC algorithm, which would be useful given the high importance of such processes for building energy consumption.

- Heat sources in the building due to internal heat release, heating or air conditioning are currently not taken into account. They could be included via a modification of the MC algorithm.

- No humid processes like humidity in the walls and the ground, evaporation from puddles on the surface, or evapotranspiration by urban vegetation can be taken into account with the current model implementation. This should be a priority for future developments to study adaptation measures to climate change in urban areas.

3 Evaluation for dry and sunny conditions at the COSMO urban-like outdoor scale model

Meso-NH-IBM has been evaluated against experimental data by Auguste et al. (2019) for 1.) the viscous flow around a circular cylinder in a wind tunnel, 2.) the turbulent flow around a surface-mounted cube in a wind tunnel, and 3.) the turbulent flow in the outdoor container array deployed in the framework of the Mock Urban Setting Test in Utah's west desert (MUST, Biltoft (2001); Biltoft et al. (2002)). These evaluation cases were with respect to neutral or near-neutral stratification. Stardis has been evaluated by Caliot et al. (2026). Heat conduction has been evaluated against results of deterministic finite difference and finite volume methods for 1.) a 1-D homogeneous slab, 2.) a 1-D slab with two homogeneous layers in thermal contact, and 3.) a 3-D thermal bridge as in a building wall.

In the present study, the coupled Meso-NH-IBM-stardis (named Meso-NH-IBM in the following) shall be evaluated against experimental data representing an urban district for non-neutral atmospheric stratification. The Comprehensive Oudoor Scale MOdel (COSMO) urban-like scale model is well suited for this purpose since it consists of concrete blocks, which mimic heat storage like in a real urban environment and there is no vegetation nor human activity. Given that moist processes are not included in the current Meso-NH-IBM, the focus is on dry and sunny conditions. In addition to the evaluation against experimental data, the COSMO site is also simulated using the established urban canopy model TEB.

https://doi.org/10.5194/egusphere-2026-2061
Preprint. Discussion started: 15 June 2026

3.1 The Comprehensive Outdoor Scale MOdel and experimental data

The COSMO physical scale model (Kanda et al., 2007) is located on the campus of the Nippon Institute of Technology in Saitama Prefecture (36.02695°N, 139.704443°E) in the northern outskirts of Tokyo metropolitan region (Japan). The terrain around the site consists of almost flat paddy fields and the distance to the nearest point on the Pacific Ocean is about 80 km (West-North-West). At the site there is a 1:50 and a 1:5 model. Only results of the 1:5 model are investigated since following Kanda et al. (2005), the 1:50 model is not similar to a real urban site in terms of thermal inertia. The 1:5 model consists of an aligned array of 1.5 m side length cubes with 1.5 m distance between each cube. The extent of the arrary is 96 m × 48 m, there are 32 × 16 cubes (512 cubes in total). The long side of the array is oriented in north-west (313° from North, clockwise) to south-east direction (133°).

The array-averaged urban morphological parameters are $\lambda_p = 0.25$, $\lambda_w = 1.0$, and $H_{\mathrm{mean}} = 1.5$ m. The same concrete material with heat conductivity ($\lambda = 1.06$ W m^{-1} K^{-1}), volumetric heat capacity ($c = 2.34 \times 10^6$ J m^{-3} K^{-1}) has been used for the 0.1 m thick cubes and for the 0.15 m thick conrete plate covering the entire ground (Kawai et al., 2007). The surfaces are covered with the same dark gray diffusive paint with broadband terrestrial infrared emissivity ($\epsilon = 0.89$), and broadband solar reflectivity ($\alpha \approx 0.1$).

Three 12 m flux towers are located on the site, in the present study only results from the central flux tower are investigated. Up- and downwelling solar and terrestrial infrared radiative flux density is measured with a frequency of 1 Hz with an Eko MR-40 radiometer at 4.5 m height (3 × H_{mean}). A Kaijo DA600 (TR90-AH) sonic anemometer with a sampling frequency of 50 Hz measures the turbulent fluxes of momentum and sensible heat at 3 m height (2 × H_{mean}) using the eddy covariance method. A vertical profile of air temperature is measured with a frequency of 50 Hz by bare thermocouples of 0.05 mm diameter each 0.2 m between 0 m and 8 m.

Thermal camera images from Morrison et al. (2018) are available for the period between June 16 2014 and September 26 2014 for the evaluation of the simulated surface temperature. The thermal cameras (Optris PI-160, Optris GmbH) output per-pixel brightness temperature (T_b) that relates to at-sensor 7-13 µm band radiance (L) that is radiometrically calibrated by the manufacturer with ±2 K accuracy. Per-pixel T_b is converted to per-pixel skin surface temperature (T_{surf}) using a modification of the method presented in Morrison et al. (2018) (Appendix B). The cameras were installed on aluminium lattice towers in 6.8 m and 7.0 m a.g.l.. The camera images are taken every 60 s, have 160 × 120 pixels with an effective resolution of 0.03 m × 0.043 m to 0.079 m × 0.111 m. The T_{surf} derived from the thermal cameras depend on the sky emissivity (ν) in the cameras spectral range accounting for differences in pyrgeometer (≈ 4 to 50 µm) and camera (7 to 13 µm) spectral response. Given the uncertainties of ν, the values of 0.28, 0.38, and 0.48 have been tested; the value of 0.38 being the most likely for the selected meteorological conditions (Idso, 1981). The surface materials ϵ also influences the derived T_{surf} and the initial paint could have altered. Therefore, values of 0.84, 0.89, and 0.94 for ϵ have been tested.

Inagaki and Kanda (2008) have shown that the roughness sublayer of the cubes extends to about 1.5 × H_{mean}. Therefore, the flux measurements at the central tower at 2 × H_{mean} are above the roughness sublayer height. Inagaki and Kanda (2010) further found that at 3 m height, the Reynolds stresses are constant with height, the mean wind profile is logarithmic, and the

https://doi.org/10.5194/egusphere-2026-2061
Preprint. Discussion started: 15 June 2026

mean flow is horizontally homogeneous, which further corroborates that the eddy-covariance measurements at $2 \times H_{\mathrm{mean}}$ are representative of the constant flux layer. Kawai and Kanda (2010) investigated the closure of the urban energy balance at the site and found that the nocturnal turbulent fluxes can be underestimated by up to 44%, especially in calm conditions with weak turbulence. During the day, the turbulent flux measurements perform well. Furthermore, Kawai and Kanda (2010) found that for all seasons, most of the net radiation is partitioned into the storage heat flux, thus the correct simulation of the heat storage in the cubes and the ground is crucial to correctly represent the surface energy balance of the COSMO site. Kawai and Kanda (2010) also found non zero latent heat fluxes at the site, which could be due to dew, stagnating rain water, or absoption of rain water by the concrete.

3.2 Selected meteorological conditions and forcing preparation

The model evaluation is conducted for a hot, sunny, and dry period from August 19 0:00 (local time) to August 22 16:00 that occurred during the time period for which thermal camera images are available. Between August 22 16:00 and August 23 0:00, high wind speed occurred, leading to invalid sensible heat flux data. Therefore, this period is not simulated. No latent heat flux measurements are available during the selected period. Fig. 4a presents the time series of the observed downwelling radiation at 4.5 m height, Fig. 4b the average air temperature observed by the thermocouples between 4 and 6 m height ($T_f(z = 5\ \mathrm{m})$), and Fig. 4cd the wind speed and direction observed by the sonic anemometer at 3 m height ($U_f(z = 3\ \mathrm{m})$ and $\gamma_f(z = 3\ \mathrm{m})$, respectively). Partitioning of the observed total downwelling solar radiation into direct and diffuse has been made by using the ratio between direct and diffuse radiation in the ERA5 data (Hersbach et al., 2020). The time series of solar radiation is characteristic of situations with few clouds with direct solar radiation reaching 700 to 850 $\mathrm{W\,m^{-2}}$ and diffuse solar radiation reaching 180 to 250 $\mathrm{W\,m^{-2}}$ around solar noon. A few clouds are present, leading to short drops of direct solar radiation at some instances. The downwelling terrestrial radiation flux density is linked to the daily cycle of near-surface air temperature. Its lowest values of 420 $\mathrm{W\,m^{-2}}$ occur at the end of the night and its highest values of about 500 $\mathrm{W\,m^{-2}}$ in the afternoon. T_f is high during the selected time period. The lowest T_f occur at the end of the night (5:00 local time) with 24 °C on August 19 and 26 °C on August 20-22. The daily maximum T_f is reached in the afternoon and lies between 35.5 °C and 36.5 °C. U_f is low during the night and morning with values below 1 $\mathrm{m\,s^{-1}}$. In the late afternoon, it rises to 2 $\mathrm{m\,s^{-1}}$ on August 19 and 20, 1.5 $\mathrm{m\,s^{-1}}$ on August 21, and above 2.5 $\mathrm{m\,s^{-1}}$ on August 22. This is due to a sea breeze reaching the site. γ_f is mostly north-west to north, but it can shift to south-east in the evening and night due to the sea breeze.

3.3 Model configuration

3.3.1 Meso-NH-IBM

In the reference configuration (REF) employed in the present study, Meso-NH-IBM is employed to simulate an array of 4 × 4 cubes (Fig. 5a) of the COSMO site with a horizontal and vertical resolution of 0.15 m. There are thus 10 grid points per cube side, which leads to a reasonable capture of the recirculation zones behind the cubes (Auguste et al., 2019). The

https://doi.org/10.5194/egusphere-2026-2061
Preprint. Discussion started: 15 June 2026

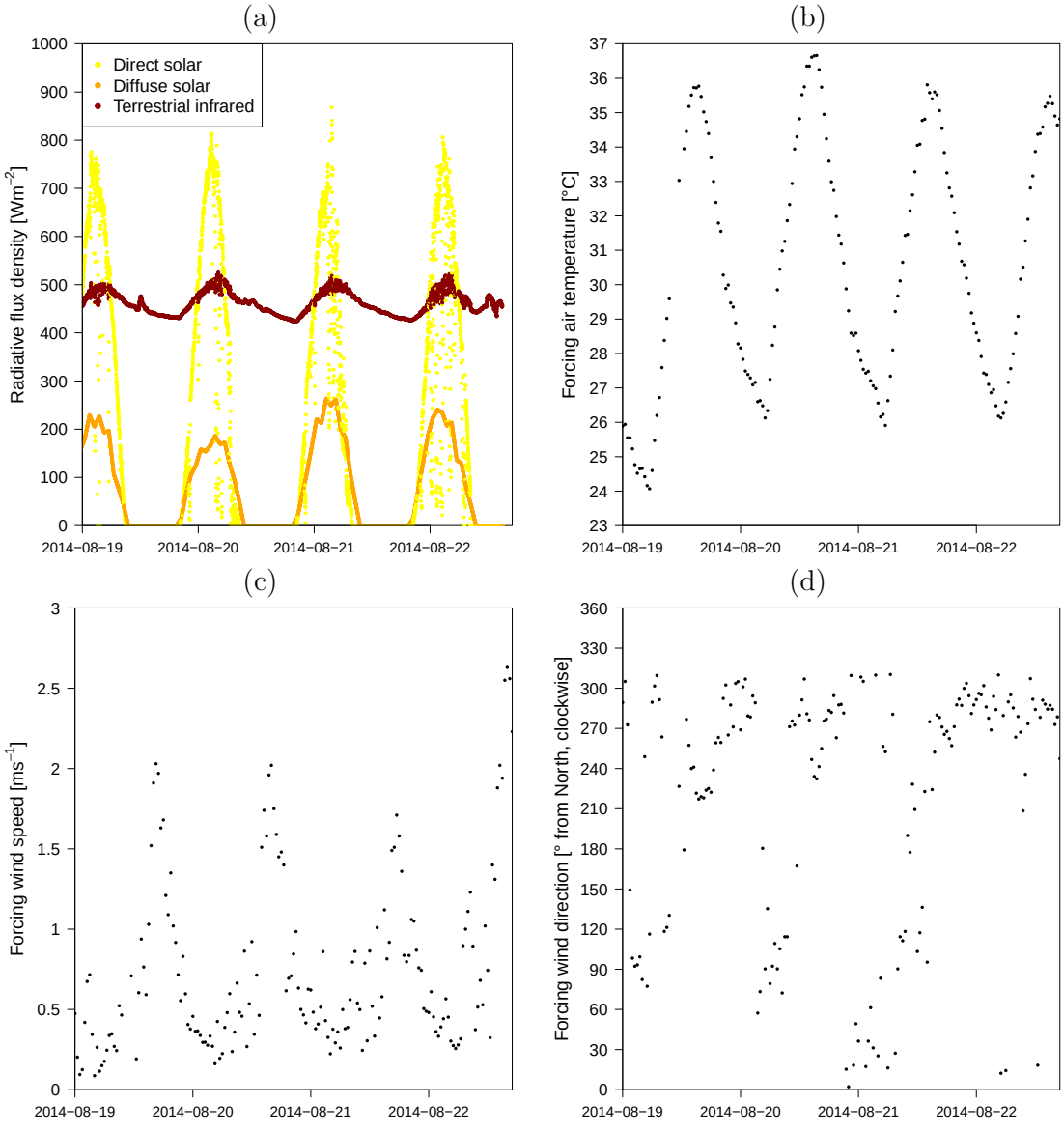

Figure 4. Time series of the meteorological forcing observed at the COSMO site and used as forcing for Meso-NH-IBM from August 19 2014 0:00 local time (August 18 15:00 UTC) to August 22 2014 16:00 local time. (a): Downwelling radiative flux density taken from the radiometers at 4.5 m height and ERA5, (b) air temperature at 5 m height taken from the thermocouples, (c) and (d): wind speed and direction at 3 m height taken from the sonic anemometer. The radiative fluxes are available each 60 s, air temperature and wind each 1800 s.

lower-left border of the domain is placed in the middle between two cubes in both x- and y-direction, the edge of the first cube is thus located at $(x = 0.75\ \mathrm{m}, y = 0.75\ \mathrm{m})$. The model domain is flat and the grid Cartesian. The horizontal extent of the domain is 12 m × 12 m (80 × 80 grid points). In the vertical direction, the grid size is kept contant (0.15 m) below a height of 3 m. At higher levels, a grid stretching with a 25% increase of vertical grid size per grid point is applied. There are

https://doi.org/10.5194/egusphere-2026-2061
Preprint. Discussion started: 15 June 2026

42 vertical grid levels, the model top is at 83.57 m height, and the vertical grid resolution reaches 15 m at the model top. No prognostic equation for water vapour mixing ratio is solved, and the Coriolis force is not taken into account. The turbulence mixing length is calculated following Honnert et al. (2021). The weighted essentially non-oscillatory discretisation of the third order (WENO3) is used since it can deal well with strong gradients (Lunet et al., 2017) as they are induced by the Immersed Obstacles. No additional numerical diffusion is activated due to the intrinsic diffusion of the WENO3 scheme. For the cube and ground, an aerodynamical roughness length of 0.002 m is taken and the wall model described by Auguste et al. (2019) is activated. Δt_{MNH} is between 0.05 s in the afternoon and evening when the wind speed is highest and 0.1 s during the night when the wind speed is lowest.

Cyclical bondary conditions are employed such that an infinite array of cubes is assumed. This is sufficient for the present study dealing with evaluation of the conductive-radiative-convective heat exchanges with stardis. However, larger coherent structures like the streaky structures with low momentum in the streamwise direction found by Inagaki and Kanda (2010) for the COSMO site cannot be represented with the 4×4 cube configuration. No attempt has been made to simulate the surroundings of the COMSO site with a coarser resolution model and to perform grid nesting to force the highest-resolution domain (as made in Nagel et al. (2022) for the MUST site). This is because of the numerous uncertain parameters related to the large-scale forcing data and the characteristics of the surrounding land cover. Instead, the Meso-NH prognostic u, v, and θ are forced above 4 m to the observed meteorological parameters above the cubes (Sect. 3.2, Fig. 4). The forcing is made via nudging with a relaxation time constant of $t_{\mathrm{rel}} = 5$ s. Given that meteorological observations are not available for the entire height of the domain, the observed data are extended in the vertical direction such as to obtain vertical profiles of forcing parameters covering the entire model height $(u_f(z), v_f(z), \theta_f(z))$. $\theta_f(z)$ is calculated based on $T_f(z = 5\ \mathrm{m})$ by assuming that it is constant with height between 4 m and 100 m (Eq. 17). $u_f(z)$ and $v_f(z)$ are calculated based on $U_f(z = 3\ \mathrm{m})$ and $\gamma_f(z = 3\ \mathrm{m})$ by assuming a logarithmic wind profile between 3 m and 100 m, and no vertical wind shear (Eq. 18 to Eq. 21).

$$\theta_f(z) = \frac{T_f(z = 5\ \mathrm{m})}{\Pi(z = 5\ \mathrm{m})} \quad \text{for } z \in [4\ \mathrm{m}, 100\ \mathrm{m}] \tag{17}$$

$$u_* = \frac{\kappa U_f(z = 3\ \mathrm{m})}{\frac{z=3\ \mathrm{m}}{z_{0,m}}} \tag{18}$$

$$U_f(z) = \frac{u_*}{\kappa} \ln\left(\frac{z}{z_{0,m}}\right) \quad \text{for } z \in [3\ \mathrm{m}, 100\ \mathrm{m}] \tag{19}$$

$$u_f(z) = -U_f(z)\ \sin(\gamma_f(z = 3\ \mathrm{m})) \tag{20}$$

$$v_f(z) = -U_f(z)\ \cos(\gamma_f(z = 3\ \mathrm{m})) \tag{21}$$

with u_* the friction velocity, $\kappa = 0.4$ the von Kármán constant, and $z_{0,m} = 0.15$ m the bulk momentum roughness length. Vertical profiles between 4 m and 100 m height of the forcing variables $u_f(z)$, $u_f(z)$, and $\theta_f(z)$ averaged over 30-minute

https://doi.org/10.5194/egusphere-2026-2061
Preprint. Discussion started: 15 June 2026

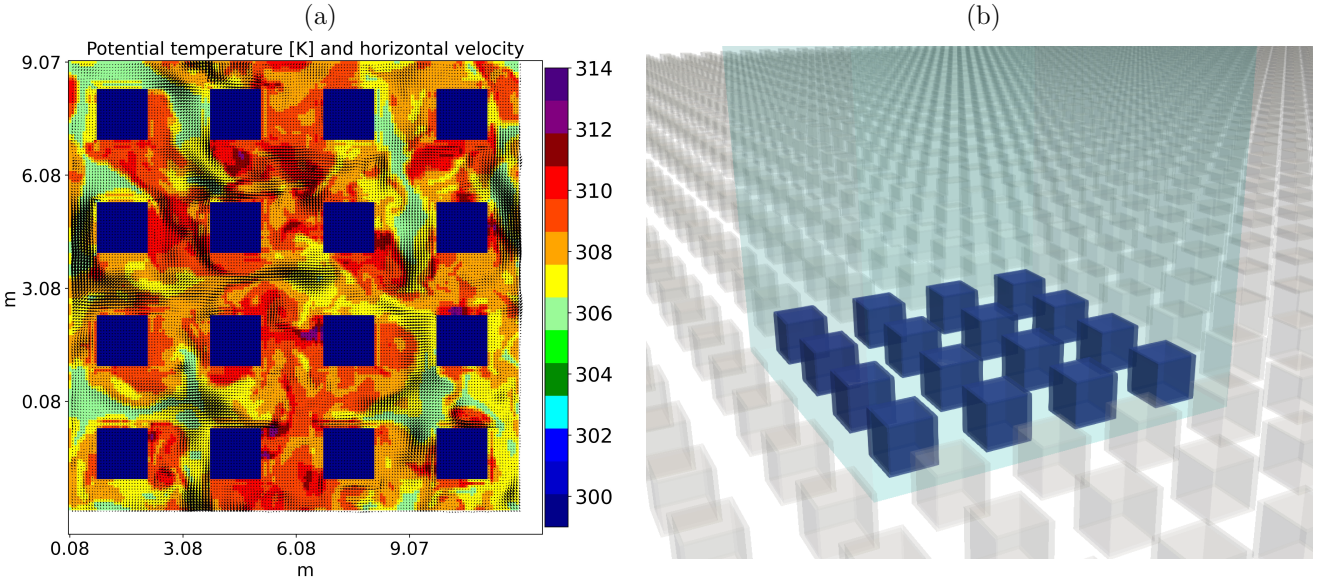

Figure 5. (a): Instantaneous field of θ, u, and v simulated by Meso-NH-IBM at $t = 43200$s in the full simulation domain covering with 4 $\times$ 4 cubes of the COSMO array. Meso-NH-IBM employs cyclical boundary conditions. (b) Embeddedness of the Meso-NH-IBM simulation domain in the stardis simulation domain which consists of a 24 $\times$ 24 cubes array to mimic an almost infinite array.

time periods are provided to Meso-NH-IBM. These are interpolated linearly in time and space in Meso-NH. Above $z = 4$ m, the domain averages of the prognostic variables ($< \Psi >$) are nudged towards the corresponding forcing variable (Ψ_f) with the relaxation time T_{rel} following

$$\frac{\Delta \Psi}{\Delta t_{\mathrm{MNH}}} = -\frac{< \Psi > - \Psi_f}{t_{\mathrm{rel}}} \tag{22}$$

By nudging the domain averaged prognostic variables, high-frequency turbulent fluctuations are less influenced by the nudging. No atmospheric radiation scheme is activated in Meso-NH-IBM. Instead, the observed downwelling direct solar, diffuse solar, and terrestrial infrared radiation are prescribed and interpolated linearly in time.

With the employed cyclical boundary conditions and forcing reconstruction between 4 m and 100 m, it is implicitly assumed that the array of cubes has an infinite extension. With this setup, the meteorological conditions simulated above about 4 m height will not match the real ones, since the internal boundary layer of the real cube array does not extend higher. However, in the current study, only the surface energy balance and the temperature profiles below 4 m height will be evaluated.

3.3.2 Stardis

The stardis simulations are fed with the meteorological forcing data at the image points in the 12 m $\times$ 12 m Meso-NH-IBM domain. The radiative and convective random paths can reach areas outside this domain. Therefore, the stardis simulation is

https://doi.org/10.5194/egusphere-2026-2061
Preprint. Discussion started: 15 June 2026

conducted for an extended cube morphology with 10 lines of cubes added in both x- and y-direction (Fig. 5b). In the case a random path reaches the surface outside the Meso-NH-IBM domain at the postion $(x_{\mathrm{out}}, y_{\mathrm{out}}, z_{\mathrm{out}})$, its position is corrected following

$$x_{\mathrm{shift}} = \max\left(\mathrm{mod}(x_{\mathrm{out}}, 12), \mathrm{mod}(x_{\mathrm{out}}, 12) + 12\right) \tag{23}$$

$$y_{\mathrm{shift}} = \max\left(\mathrm{mod}(y_{\mathrm{out}}, 12), \mathrm{mod}(y_{\mathrm{out}}, 12) + 12\right) \tag{24}$$

$$z_{\mathrm{shift}} = z_{\mathrm{out}} \tag{25}$$

with mod denoting the modulo operation. This position shift assumes the same flow is present in adjacent 4x4 cube groups. A ground body of 10 m depth made of the same material as the cubes is simulated in stardis. This differs from the real site for which the concrete plate extends to only 0.15 m depth. The material parameters for the cubes and the ground body are 1.06 $\mathrm{W\,m^{-1}\,K^{-1}}$ for heat conductivity (λ), 2340 $\mathrm{kg\,m^{-3}}$ for density (ρ_m), 900 $\mathrm{J\,kg^{-1}}$ for specific heat capacity (c_m)), 0.89 for ϵ, and 0.14 for α. α is set to a higher value than the one ($\alpha = 0.11$) reported by Kawai et al. (2007), since dirt, moss, and lichens have altered the initial painting of the cubes and ground. Simulations have been conducted with HTRDR-Urban (Caliot et al., 2023) for the selected time period to test which α yields the best results for the observed upwelling solar radiation. The best results are obtained for $\alpha = 0.14$ intead of $\alpha = 0.11$ (not shown). The surface roughness multiplier (z_{rough}) in the calculation of the exchange coefficients is set to 1.52, the value for concrete [1]. It is assumed that all surfaces are Lambertian.

Initial values need to be prescribed for the temperature of the different solids (cube top, cube walls, ground), and the interior air temperature. These are taken from a TEB simulation (Sect. 3.3.3) that is started on August 16 0:00. The solid temperatures simulated by TEB on August 19 0:00 are taken as initial values for stardis. The initial values are 309.2 K for the cube top, 310.6 K for the cube walls, 310.2 K for the ground body, and 312.1 K for the interior air temperature. The value of the ground body initial temperature of 310.2 K is imposed as Dirichlet boundary condition at the bottom of the ground body in 10 m depth. Zero heat flux Neumann boundary conditions are imposed at the lateral boundaries of the ground body. The reinjection length (δ_b) used in the conduction algorithm (Caliot et al., 2024) is set to $\delta_b = 0.004$ m. This means that a linear temperature profile between the surface of the solids and a depth of 0.004 m in the solid is assumed.

The number of realisations of the MC simulations (N) is set to 2000 for each probe point between 6:00 and 18:00 local time and to 1000 otherwise. This is because the largest random fluctuations in the MC simulations are due to the solar radiation.

3.3.3 Simulations with the urban canopy model Town Energy Balance TEB

Since the geometry of the COSMO site is simple, it can be simulated with the TEB urban canopy model without introducing many uncertainties compared to Meso-NH-IBM. The TEB urban morphology parameters and material characteristics are set exactly the same as those of the COSMO site, the building energy model in TEB is configured such as to have neither heating, air conditioning, ventilation, nor infiltration. Rain in the forcing data is set to zero. The calculation of the exchange coefficients for sensible heat have been rendered identical to those in Appendix A. The only shortcoming of TEB is that it assumes a

[1] https://bigladdersoftware.com/epx/docs/8-1/engineering-reference/page-020.html

https://doi.org/10.5194/egusphere-2026-2061
Preprint. Discussion started: 15 June 2026

street canyon instead of a cube urban geometry. Uniform orientation of the street canyon is assumed. The TEB simulations are conducted from August 16 0:00 local time to August 22 23:00 local time. The TEB results are compared to the Meso-NH-IBM ones in Sect. 4.

3.4 Sensitivity of results to choices in the model configuration

The Meso-NH-IBM simulations are conducted with 7 different model configurations:

- The reference simulation (REF) is made as described in Sect. 3.3 with $\Delta t_{\mathrm{FRC}} = 60$ s, and $\Delta t_{\mathrm{STA}} = 300$ s.
- Two simulations (DL2 and DL8) are made with the reinjection length in stardis modified to $\delta_b = 0.002$ m and $\delta_b = 0.008$ m, respectively.
- The MTO300 simulation is made with a less frequent writing of the meteorological forcing data ($\Delta t_{\mathrm{FRC}} = 300$ s).
- The STD60 simulation is made with more frequent calculation of conductive-radiative-convective heat exchanges ($\Delta t_{\mathrm{STA}} = 60$ s).
- For the 20P simulation, the Meso-NH-IBM grid resolution (Δ) is refined by a factor of 2 to 0.075 m or 20 grid points per cube side. For this simulation, Δt_{MNH} also needs to be reduced by a factor of 2. The horizontal grid is 160 $\times$ 160 points, and the number of vertical grid points is 66.
- For the 4REA simulation, the number of realisations in the MC algorithm (N) is increased by a factor of 4 to 8000 (6:00 to 18:00 local time) and 4000 (18:00 local time to 6:00 local time). This allows to test whether the convergence of the MC algorithm is correct. The standard deviation of the individual probe surface temperatures should decrease by a factor of 2 when N is increased by a factor of 4. The results for the convergence of the algorithm will be presented in Sect. 5.2.

4 Results

4.1 Sensible heat flux

Fig. 6 shows the time series (1800 s averages) of the simulated and observed sensible heat flux (H) for the 20P configuration. The observed H lies between 20 $\mathrm{W\,m^{-2}}$ and 50 $\mathrm{W\,m^{-2}}$ during the night and reaches 180 to 200 $\mathrm{Wm^{-2}}$ during the day. The positive nocturnal H values are consistent with what can be expected in a real urban environment, which shows that the COSMO scale model surface energy balance resembles that of a real urban area. Valid observed H data are not available for all instances and they can show considerable fluctuations. The numerical models Meso-NH-IBM and TEB simulate almost the same values of H. Compared to the observations, they simulate slightly higher H during the night. This could be due to the underestimation of H by the eddy covariance measurements for the nocturnal low speed wind conditions. Both numerical models also simulate slightly higher values of H around noon during the first two days. This could be due to residual humidity from previous rainy periods that is not taken into account by the numerical models. No systematic overestimation of H by the

https://doi.org/10.5194/egusphere-2026-2061
Preprint. Discussion started: 15 June 2026

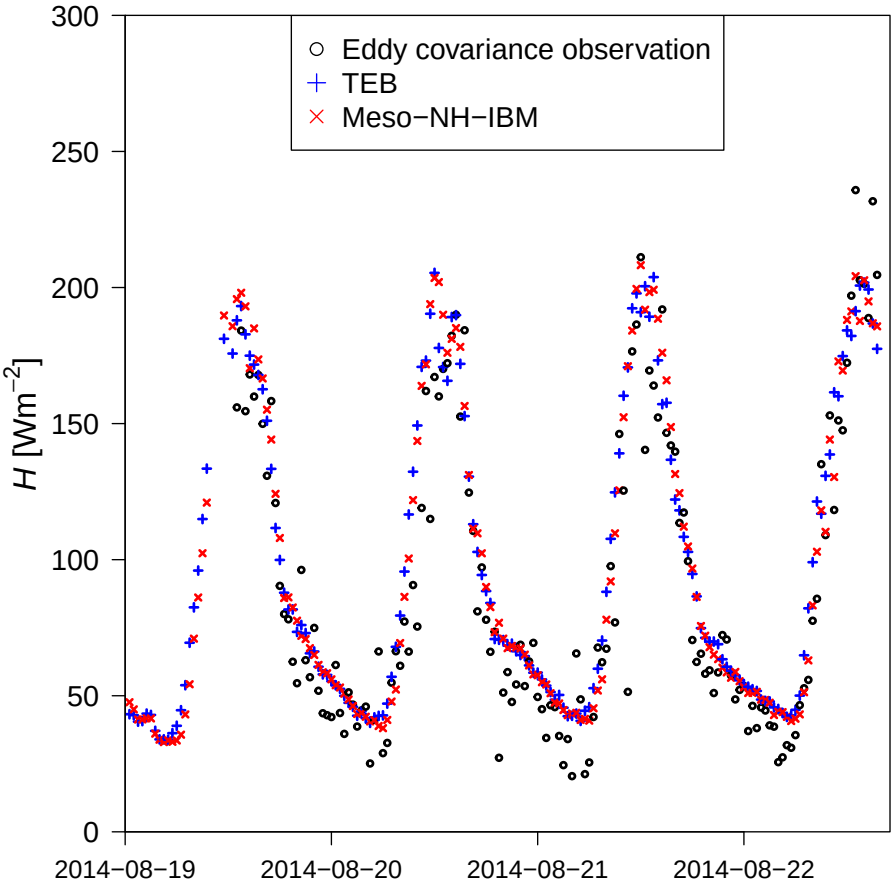

Figure 6. Time series of the sensible heat flux (H) observed via the eddy covariance method and simulated with the urban canopy model Town Energy Balance (TEB) and the building-resolving model Meso-NH-IBM for the 20P configuration.

numerical models is found at noon during the last two days.

https://doi.org/10.5194/egusphere-2026-2061
Preprint. Discussion started: 15 June 2026

Fig. 7 displays the time series of H simulated by Meso-NH-IBM for the REF, 20P, DL2, DL8, MTO300, and STD60 model configurations. The differences between the REF configuration and those with different reinjection distances in stardis (DL2, and DL8) or those with different Δt_{FRC} (MTO300) or Δt_{STA} (STD60) are very small, which is an important hint that the coupled Meso-NH-IBM stardis results are robust against changes in these parameters. However, all configurations with the coarser grid resolution in Meso-NH-IBM (REF, DL2, DL8, MTO300, and STD60) simulate about 5% higher H values at noon compared to the 20P configuration. Given the comparison with TEB and the observations (Fig. 6), it can be concluded that the coarser grid resolution in Meso-NH-IBM slightly deteriorates the results around noon. This is consistent with Auguste et al. (2019) who showed that Meso-NH-IBM agrees better with experimental data for the flow around a surface-mounted cube when 20 or even 40 grid points per cube side length are used instead of 10. Therefore, the slightly better results for 20P compared to REF might be due to the better simulation of the prognostic atmospheric variables by Meso-NH-IBM. Given the very high computational demand for the 20P configuration it is however unrealistic that such a high resolution (e.g. $\Delta = 0.25$ m for the simulation of a low-rise residential district with $H_{\mathrm{mean}} = 5$ m) would be used in urban climate modelling applications.

4.2 Comparison of skin surface temperature and exchange coefficient between Meso-NH-IBM and TEB

The simulated H depends on the simulated exchange coefficient for sensible heat (c_H), forcing air temperature (T), and surface temperature (T_{surf}). The time series of these parameters are displayed in Fig. 8 for Meso-NH-IBM (20P configuration) and TEB. For TEB, the displayed values represent one single computational node whereas for Meso-NH-IBM they represent the average of all image or probe points corresponding to the different facets. These facets are defined as the cube tops ($z_{\mathrm{probe}} = 1.5$ m), the cube walls ($0\ \mathrm{m} < z_{\mathrm{probe}} < 1.5$ m), and the ground ($z_{\mathrm{probe}} = 0$ m). The time series of T_{surf} for the cube top and the ground agree almost perfectly between TEB and Meso-NH-IBM. The T_{surf} of the cube walls is 3 to 4 K higher for the time period around noon with Meso-NH-IBM than with TEB. This could be due to the cube orientation. Given the rotation of the cube sides by 47° left of the South-North axis, the sun in the South almost optimally irradiates the cube walls around noon. This might lead to the higher average T_{surf} for the cube walls for Meso-NH-IBM than for TEB, which assumes a street canyon with random orientation. The T of the cube top and cube walls seen by Meso-NH-IBM is almost equal to the one seen by TEB, except for the period around noon with the strongest solar irradiation. During this period, T is 1 to 2 K higher with Meso-NH-IBM than with TEB. This is because in the obstacle-resolving Meso-NH-IBM, the forcing is taken from the grid point adjacent to the very hot surfaces whereas with TEB the forcing is further away from the surface. The c_H at the ground is almost the same in Meso-NH-IBM and in TEB. For the cube walls, it is slightly lower during the day in Meso-NH-IBM than in TEB. This is due to a lower average wind speed close to the cube walls in Meso-NH-IBM than in TEB. For c_H at the cube top, Meso-NH-IBM and TEB agree well during the night and morning. However, 20% higher values of c_H are simulated by Meso-NH-IBM than by TEB in the afternoon. This is because the sea breeze (Fig. 4) flow is accelerated close to the cube tops in Meso-NH-IBM (Fig. 2), which cannot be represented with TEB.

https://doi.org/10.5194/egusphere-2026-2061
Preprint. Discussion started: 15 June 2026

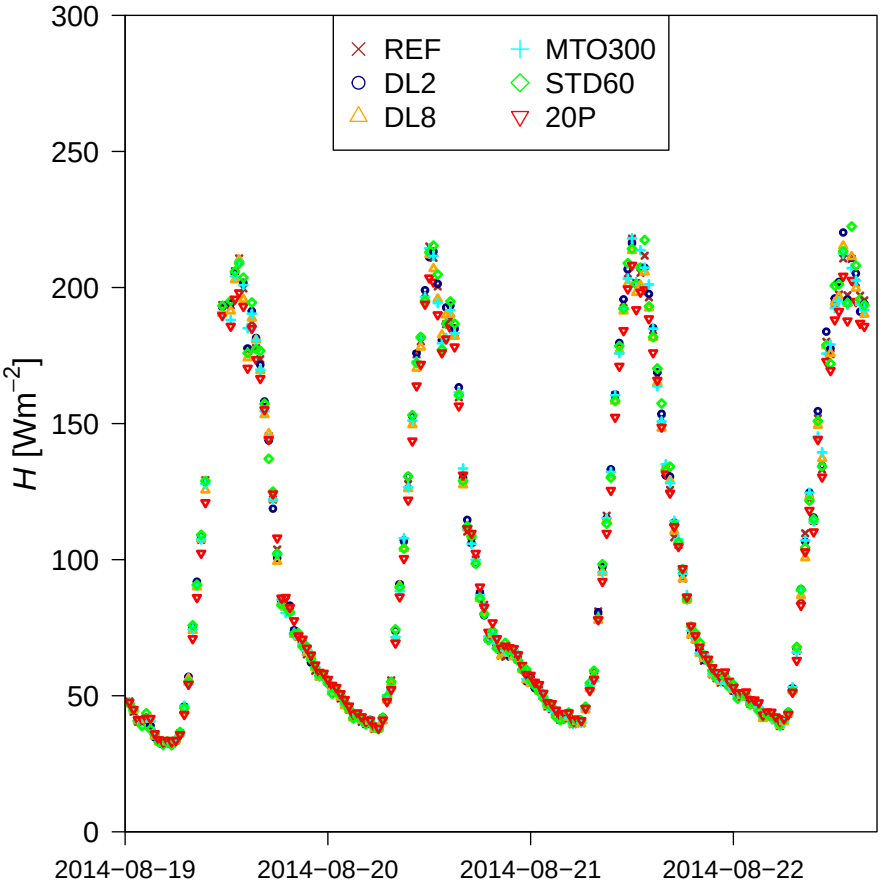

Figure 7. Time series of the sensible heat flux (H) simulated by Meso-NH-IBM with different model configurations. REF corresponds to $\Delta = 0.15$ m, $\Delta t_{\mathrm{FRC}} = 60$ s, $\Delta t_{\mathrm{STA}} = 300$ s, and $\delta_b = 0.004$ m. For DL2 and DL8, δ_b is set to 0.002 m and 0.008 m respectively. For MTO300, Δt_{FRC} is set to 300 s. For STD60, Δt_{STA} is set to 60 s. For 20P, Δ is set to 0.075 m.

4.3 Vertical profiles of air temperature

Time averages over 30 minutes of the simulated and observed vertical θ profiles are calculated and displayed for different times of the day for August 19 2014 (Fig. 9), August 20 2014 (Fig. 10), and August 21 2014 (Fig. 11). The Meso-NH-IBM results are displayed for the REF, MTO300, STD60, and 20P configurations. The results for the DL2 and DL8 configurations are not shown since they do not differ from those of the REF configuration. Observed and simulated θ decrease with height during both daytime and nighttime. This is consistent with the positive H for all times of the day (Fig. 6) for the urban-like COSMO scale model. The observed θ difference between 5 m and just above the ground is about 1 K in the nighttime and 2-3 K between 12:00 and 16:00 when H is highest. The observed θ profiles often display a relatively linear increase between 3 to 4 m and the surface and do not always show a marked inflection point around the height of the cubes. However, there are exceptions. For some instances, θ increases between 3 to 4 m and 1.5 m (the cube height), remains constant between 1.5 m

https://doi.org/10.5194/egusphere-2026-2061
Preprint. Discussion started: 15 June 2026

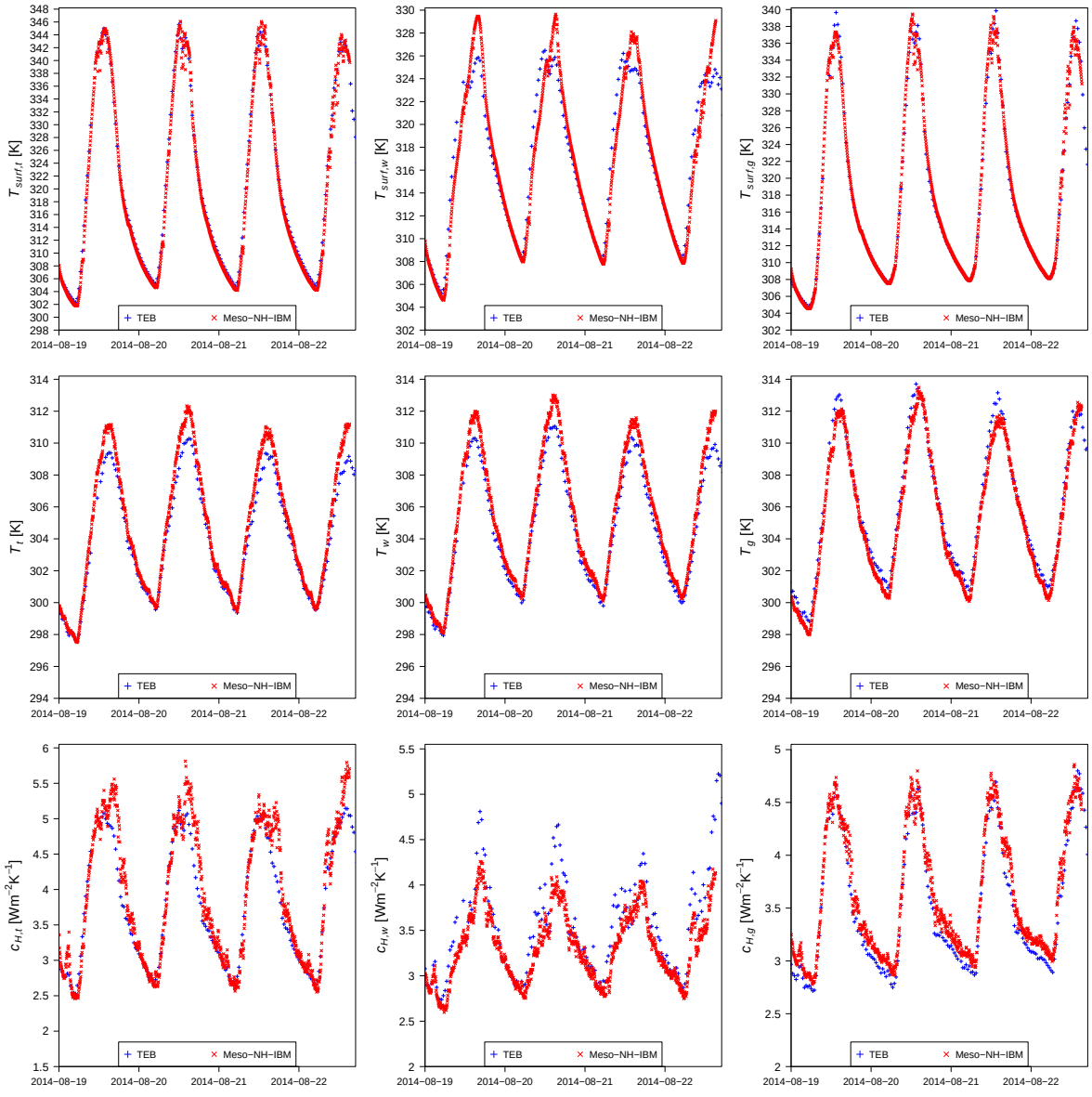

Figure 8. Time series of the surface temperature (T_{surf}), forcing air temperature (T) and exchange coefficient for sensible heat (c_H) simulated by the urban canopy model Town Energy Balance (TEB) and the building-resolving model Meso-NH-IBM (20P configuration) for the cube tops ($T_{\mathrm{surf},t}$, T_t, $c_{H,t}$), the cube walls ($T_{\mathrm{surf},w}$, T_w, $c_{H,w}$), and the ground ($T_{\mathrm{surf},g}$, T_g, $c_{H,g}$).

and about 0.5 m, and starts to increase again below 0.5 m. The most marked examples are August 19 16:00 and 18:00, August 20 0:00, 2:00, 10:00, and 20:00, August 21 10:00, 12:00, and 16:00. The phenomenon therefore occurs during both the night- and the daytime. For all three days, the observations show the formation of an inversion around 8:00. The cube tops and the

https://doi.org/10.5194/egusphere-2026-2061
Preprint. Discussion started: 15 June 2026

upper parts of the cube walls seem to heat the air between 1 and 2 m height, leading to a local maximum of θ at the height of the cubes. The atmospheric stratification becomes stable below the cube height.

The simulated θ profiles generally agree with the observed ones. Similar to the observations, θ most frequently increases almost linearily between 3-4 m and the ground. However, as in the observations, there are instances when θ becomes almost constant with height between 0.5 m and 1.5 m. Discrepancies between the simulated and observed profiles sometimes arise because the model simulates a constant θ between 0.5 m and 1.5 m, but the observations dont, and vice-versa. This might not be due to a model deficiency but only due to internal variability of the wind and temperature that cannot be timed correctly by the model.

A clear deficiency of Meso-NH-IBM is identified. It does not capture the formation of the local maximum in θ around the cube height around 8:00 and the formation of a stable stratification in the air layer below the cube height. The reason for this deficiency of Meso-NH-IBM could be that a much finer vertical resolution is required to reproduce this feature. However, only little difference is found between the results at finer resolution (20P) and the REF ones. Another potential reason is the neglect of atmospheric scattering and absorption by stardis. The warm surfaces on the cube sides might heat the air in between the cubes due to the absorption of terrestrial infrared radiation by the air, which cannot be represented by the current model version.

No relevant differences between the simulated vertical profiles are found for the different model configurations.

https://doi.org/10.5194/egusphere-2026-2061
Preprint. Discussion started: 15 June 2026

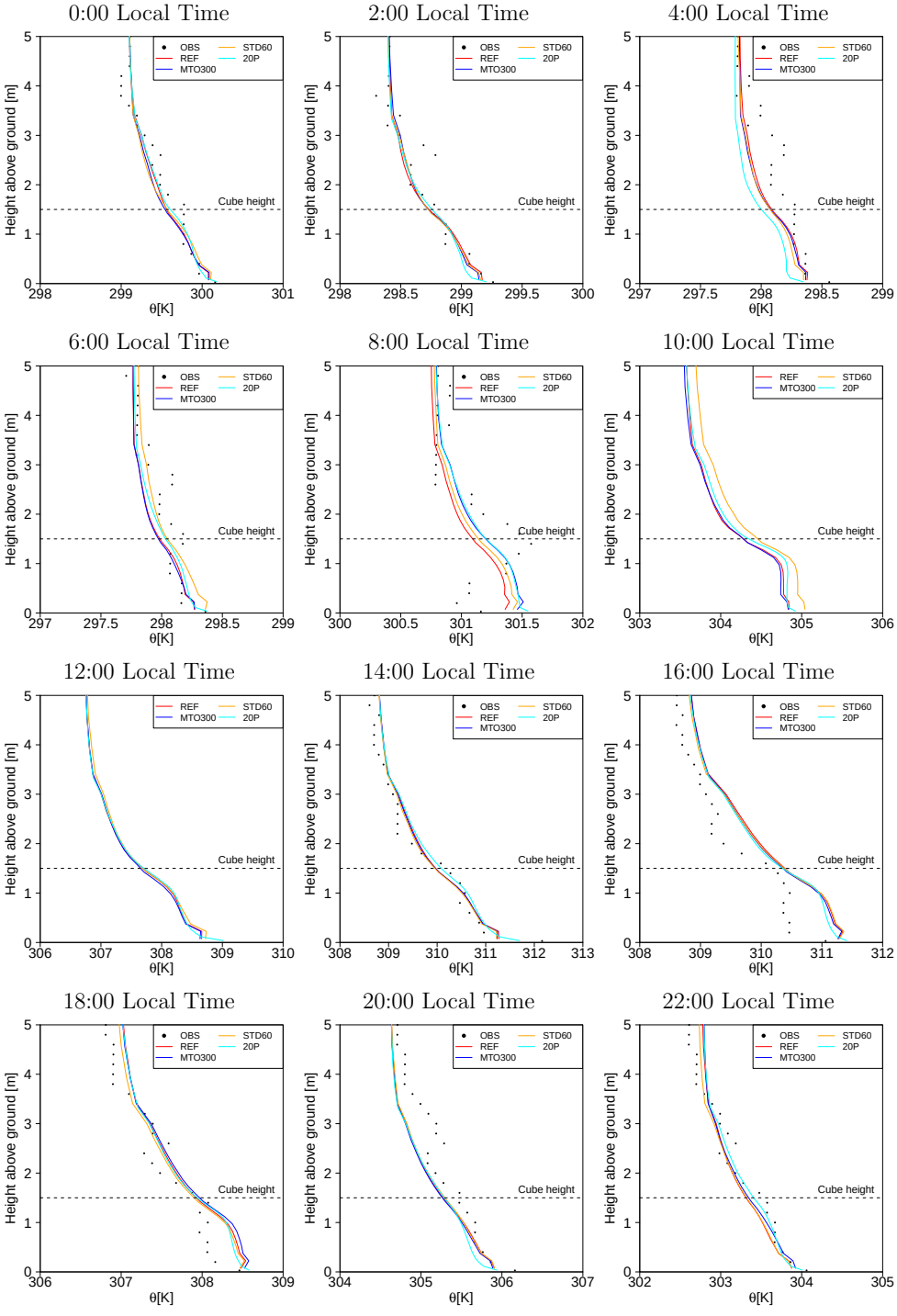

Figure 9. Vertical profiles of potential temperature (θ) simulated by Meso-NH-IBM and observed by the thermocouples (OBS) for August 19 2014. The simulated and observed values are averaged for the 30-minute time interval centered on the displayed time. No observations are available for 10:00 and 12:00 local time.

https://doi.org/10.5194/egusphere-2026-2061
Preprint. Discussion started: 15 June 2026

4.4 Thermal camera images of surface temperature

Stardis is used to render the thermal camera images from the position of the cameras with their specific resolution and field of view with 4000 samples per pixel. The meteorological forcing from the 20P configuration is used. Stardis has been modified such as to set the emissivity of the ground surfaces to $\epsilon = 1$ at the first contact of the radiative random paths (starting at the camera position) with the geometry. This allows to obtain the material surface temperature (T_{surf}) instead of T_b. The simulated values are compared with the T_{surf} obtained form the thermal cameras for different values of ϵ and ν (Appendix B). The images are compared for August 21 2024 at different times of the day with thermal camera C26 (Fig. 12) and C57 (Fig. 13) for $\epsilon = 0.89$ and $\nu = 0.38$, which are the most plausible values of these parameters. No camera value is provided for the cubes edges since the algorithm to convert the observed T_b to T_{surf} is not reliable there.

During the night, the cube top is the coolest for both stardis and the thermal cameras, which is due to the sky-view factor of 1. The sides of the cube tops and especially the edges of the roof tops exhibit the lowest simulated T_{surf}. The cameras also show this feature. The cube walls exhibit the highest T_{surf} during the night since their sky view factor is quite low. The ground T_{surf} is in between the cube top and the cube wall T_{surf}. At the beginning of the night (especially at 22:00 local time), the coolest (warmest) surfaces on the ground are those that have been in the shade (in the sun) during the late afternoon. Both stardis and the cameras show this feature. At the end of the night (e.g. 4:00 local time), the highest T_{surf} are found in the corner between the wall and the ground since here the sky-view factor is minimal, thus limiting radiative cooling. Overall the agreement between stardis and the cameras is good during the night; the differences are within 2 K. The camera values for T_{surf} of the cube tops can differ by about 2 K for different cubes, which is probably due to the dirt or moss that is present there. After sunrise, the sunlit cube sides heat quickly (especially at 6:00) and after 8:00 the cube tops and the sunlit areas on the ground heat rapidly. Stardis represents very well the temporal evolution of the sunlit and shaded areas on the cube walls and the ground. However, after 10:00 the simulated T_{surf} become considerably higher than the corresponding camera values. The difference can become as large as 10 K for some roofs at 12:00 and 14:00. The thermal camera values can differ by 5 K between different roofs, thus showing that there is some uncertainty related to these values.

During the daytime, the highest T_{surf} are simulated at the edges between the sunlit wall and the roof and the lowest T_{surf} in the corners between the bottom of the shaded walls and the shaded ground. Both stardis and the camera images show this feature.

https://doi.org/10.5194/egusphere-2026-2061
Preprint. Discussion started: 15 June 2026

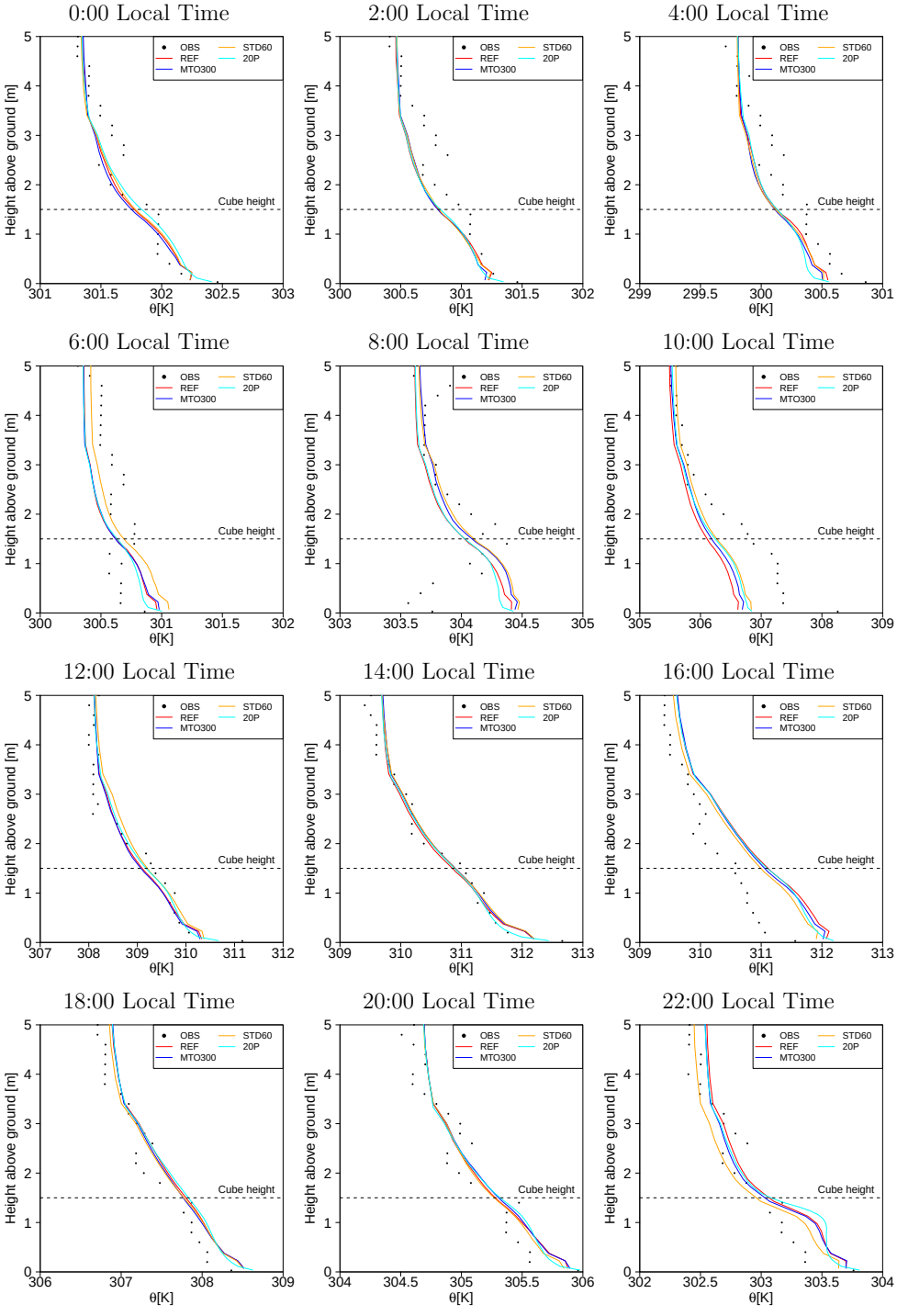

Figure 10. Vertical profiles of potential temperature (θ) simulated by Meso-NH-IBM and observed by the thermocouples (OBS) for August 20 2014. The simulated and observed values are averaged for the 30-minute time interval centered on the displayed time.

https://doi.org/10.5194/egusphere-2026-2061
Preprint. Discussion started: 15 June 2026

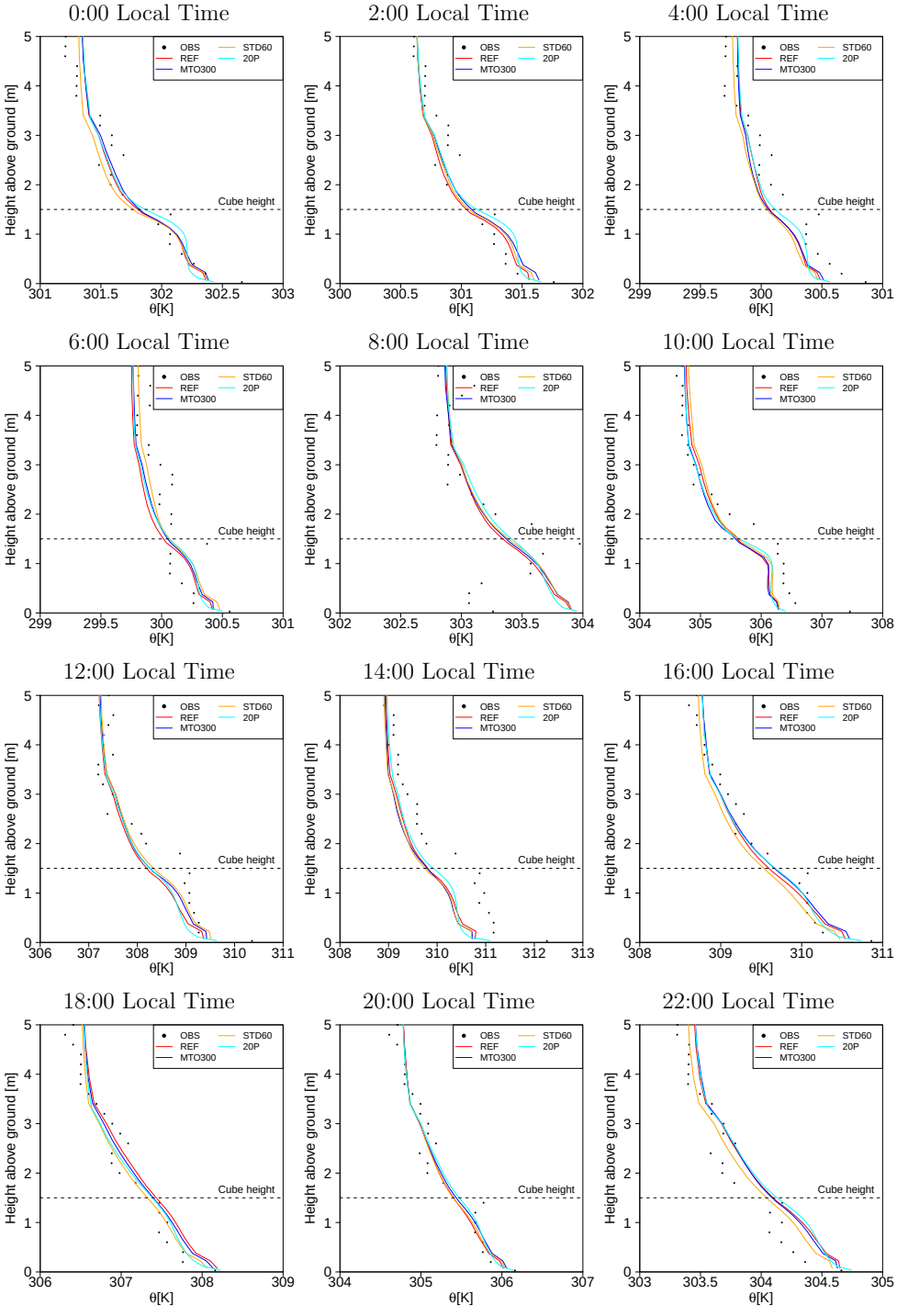

Figure 11. Vertical profiles of potential temperature (θ) simulated by Meso-NH-IBM and observed by the thermocouples (OBS) for August 21 2014. The simulated and observed values are averaged for the 30-minute time interval centered on the displayed time.

https://doi.org/10.5194/egusphere-2026-2061
Preprint. Discussion started: 15 June 2026

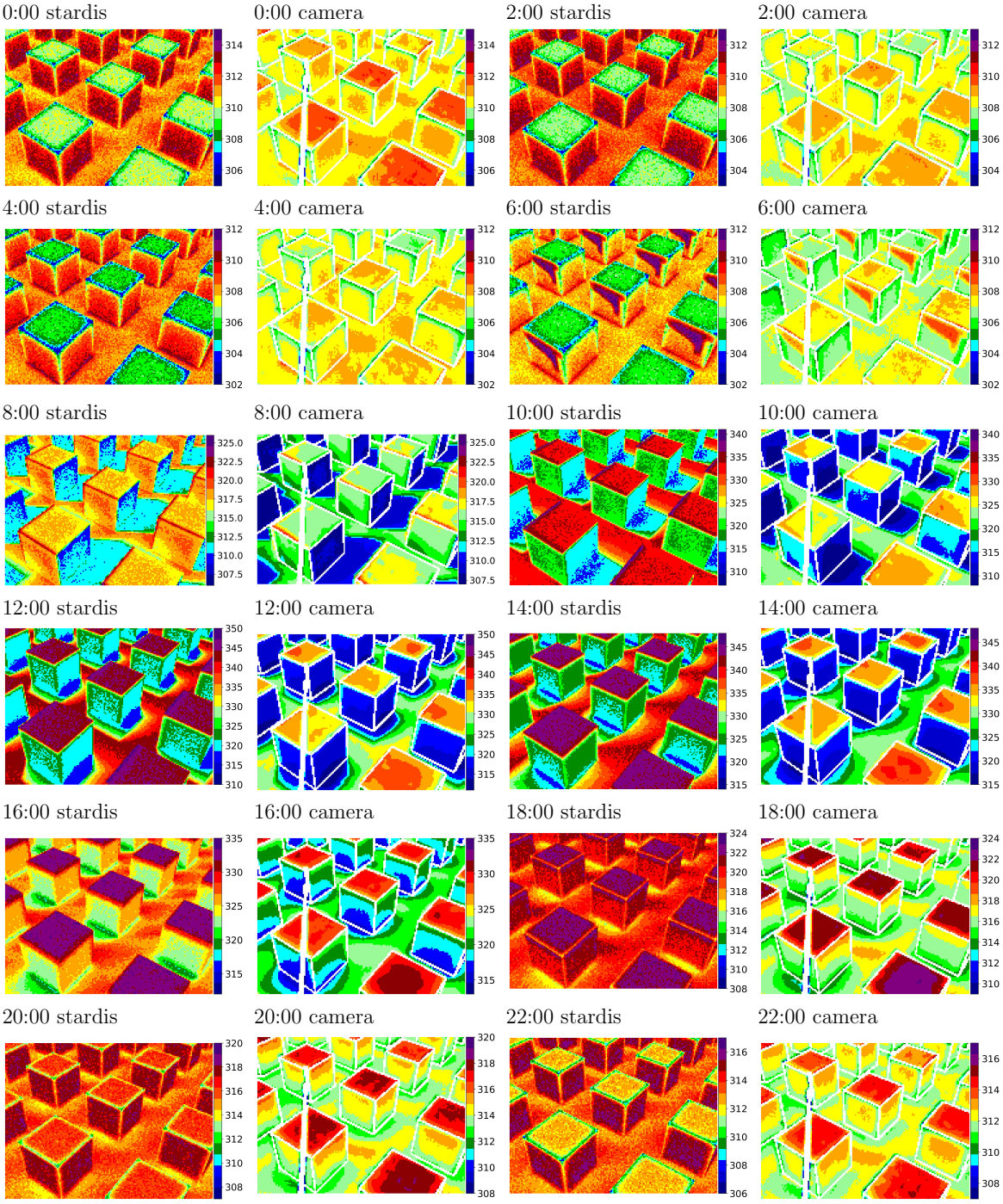

Figure 12. Rendering of the skin surface temperature with stardis using the meteorological forcing from the 20P configuration and comparison with the skin surface temperature derived from the observations with thermal camera C26 for August 21 2014.

https://doi.org/10.5194/egusphere-2026-2061
Preprint. Discussion started: 15 June 2026

To analyse the sensitivity of T_{surf} derived from the thermal camera observations on ϵ and ν, the time series of T_{surf} averaged over the pixel from the camera images belonging to the cube tops, the cube walls, and the ground simulated by Meso-NH-stardis and observed by the cameras are shown in Fig. 14 for 9 combinations of plausible ϵ (0.84, 0.89, and 0.94) and ν (0.28, 0.38, 0.48). The results show that around noon, the T_{surf} values simulated for the cube top, cube sides, and the ground are higher than what can be explained by the uncertainty of the thermal camera values. For the other times of the day, the simulated T_{surf} values lie inside the range of observed T_{surf}.

https://doi.org/10.5194/egusphere-2026-2061
Preprint. Discussion started: 15 June 2026

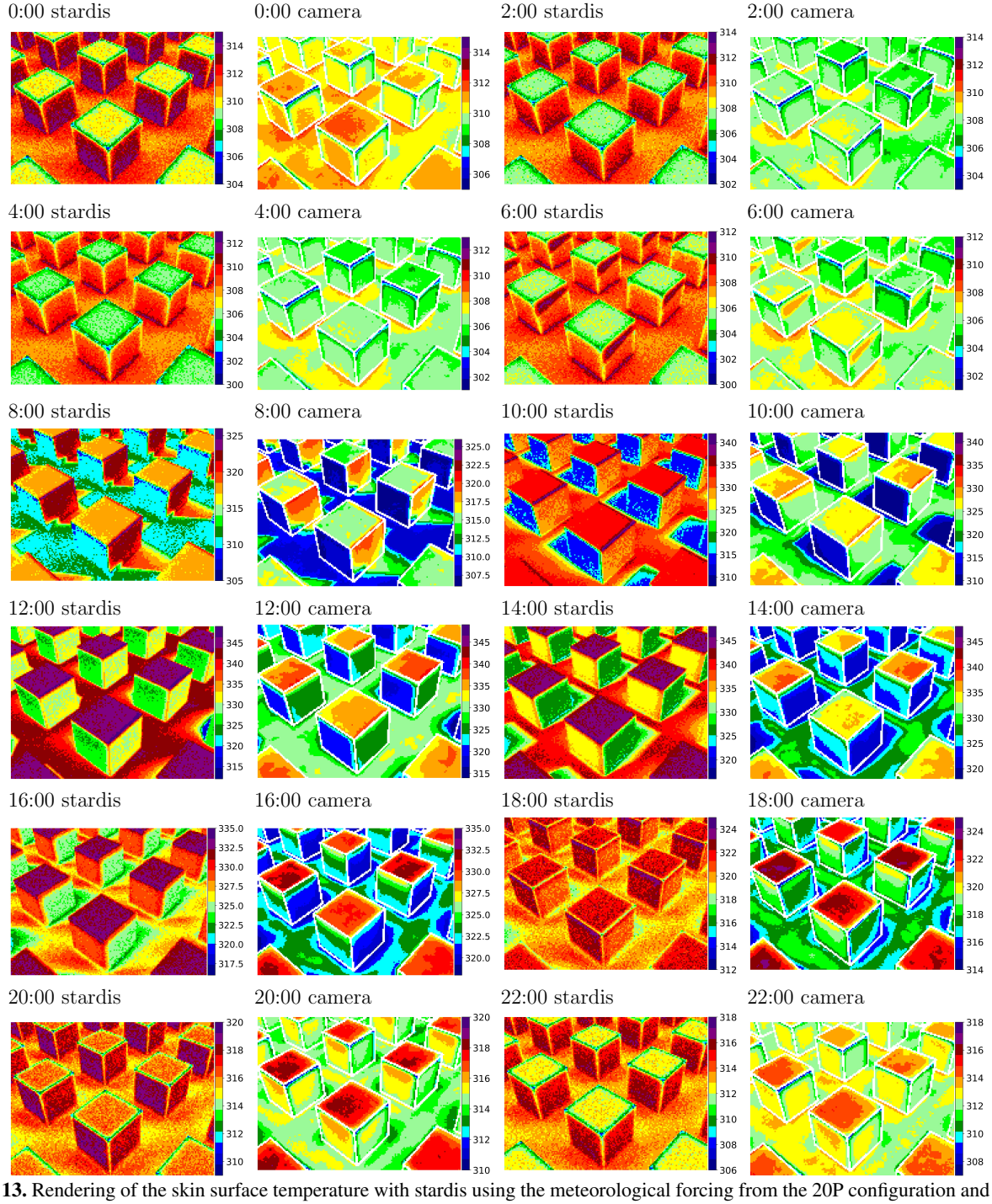

Figure 13. Rendering of the skin surface temperature with stardis using the meteorological forcing from the 20P configuration and comparison with the skin surface temperature derived from the observations with thermal camera C57 for August 21 2014.

https://doi.org/10.5194/egusphere-2026-2061
Preprint. Discussion started: 15 June 2026

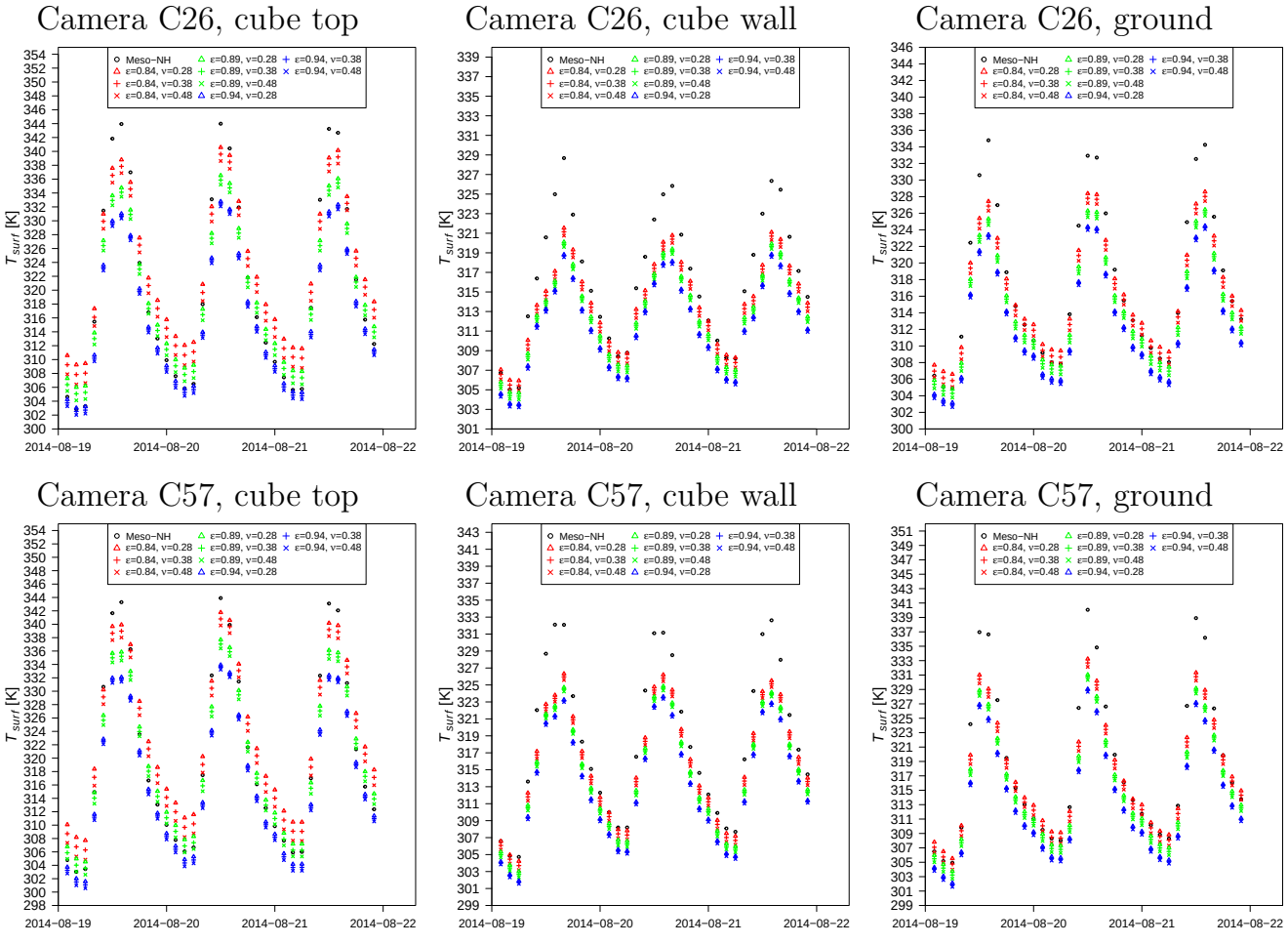

Figure 14. Time series of average T_{surf} on the cube tops, the cube walls, and the ground in the thermal cameras's field of view simulated by Meso-NH-IBM and observed by the thermal cameras. For the thermal cameras, different values of the surface emissivity (ϵ) and the sky emissivity (ν) have been used to derive T_{surf} from T_b.

https://doi.org/10.5194/egusphere-2026-2061
Preprint. Discussion started: 15 June 2026

5 Discussion

5.1 Results of model evaluation

Evaluation of Meso-NH-IBM coupled to stardis for the dry hot period at the COSMO site has shown that the time series of H and the vertical profiles of θ in the urban roughness sublayer are well simulated. A noted exception is the period after sunrise when the highest θ values are observed around the height of the cubes and lower ones below, which Meso-NH-IBM does not reproduce. A higher resolution might be necessary to capture this phenomenen. Another potential reason is the neglect of the interaction of infrared radiation with air in the urban canopy layer in stardis. The evaluation against the thermal camera images shows that stardis captures well the interaction of radiation with the geometry. However, higher than observed values of T_{surf} are simulated around noon.

Sensitivity studies with different model configurations have been made to demonstrate that the results are insensitive to settings related to the coupling. These are the frequency for writing the meteorological forcing data, the time for updating the surface temperature, and the re-injection distance used for the heat conduction in stardis. Increasing the resolution of Meso-NH-IBM from 10 points per cube side to 20 points per cube side leads to slightly better results, which is consistent with Auguste et al. (2019) who showed that the flow around a single cube is better simulated with 20 points per cube side than with 10.

A relatively large difference between the T_{surf} simulated by Meso-NH-IBM and the observed T_{surf} by the thermal cameras is found around noon. Here the simulated T_{surf} are overestimated by 5 to 10 K. The comparison between Meso-NH-IBM and the TEB results shows that this is not due to a shortcoming of the MCM or the coupling, since for the cube top, almost the same T_{surf} are simulated by the two models which are based on very different methods. The difference in T_{surf} compared to the thermal cameras is therefore probably due to the material characteristics (e.g. ϵ) or the exchange coefficient (c_H), which is shared by both models.

5.2 Convergence of the Monte-Carlo algorithm

The convergence of the MC algorithm is quantified by investigating the standard deviation of skin surface temperature (σ_T) calculated for the REF configuration and the 4REA configuration for which N has been increased by a factor of 4 compared to REF. The time series of the average values of σ for the cube tops (σ_{Tt}), the cube walls (σ_{Tw}), and the ground (σ_{Tg}) are displayed in Fig. 15. For all facets, discontinuities of σ with a decrease of a factor of $\sqrt{2}$ at 6:00 local time and an increase of a factor of $\sqrt{2}$ at 18:00 local time is found. This can be expected given the factor of 2 higher number of N between 6:00 and 18:00 local time. For the REF configuration, σ lies between 0.3 and 0.5 K during the nighttime and can reach 0.7 to 0.8 K during the daytime. The solar irradiation during the daytime causes the higher σ values then. In hindsight, the higher number of N could have been maintained until 20 or 22 local time since high σ values prevail between 18:00 and 22:00 local time. The convergence of the Monte-Carlo algorithm is excellent, since the σ values for 4REA are almost exactly a factor of 2 lower than those for REF.

https://doi.org/10.5194/egusphere-2026-2061
Preprint. Discussion started: 15 June 2026

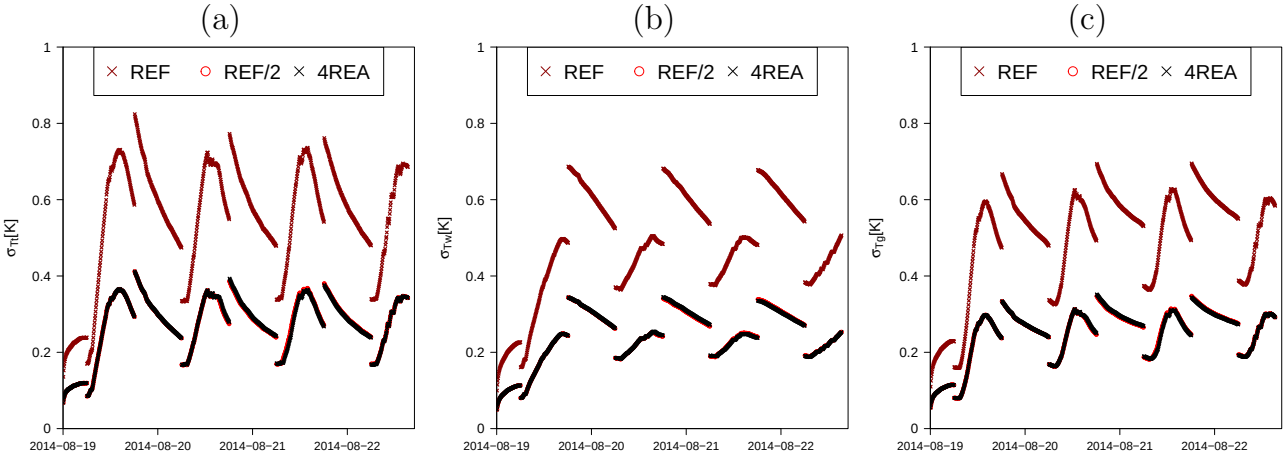

Figure 15. Time series of the standard deviation of the skin surface temperature calculated by stardis averaged over the cube top (σ_{Tt}), the cube walls (σ_{Tw}), and the ground (σ_{Tg}). For the REF configuration, the number of samples is 2000 from 6:00 to 18:00 local time and 1000 from 18:00 local time to 6:00 local time. For the 4REA configuration, the number of samples has been multiplied by 4. REF/2 denotes the σ values from the REF configuration divided by 2. Good convergence of the MC algorithm is achieved when σ is reduced by a factor of 2 for a factor of 4 higher number of realisations.

5.3 Computational cost and its resolution dependency

The computational cost has been quantified for the different configurations in terms of wall-clock time and total cpu time as reported by the Slurm Workload Manager (Tab. 1). The total CPU time is the wall-clock time multiplied by the number of computational nodes and 128 tasks for each node. All stardis simulations have been conducted on 10 nodes. The Meso-NH simulations have been conducted on 2 nodes, except for the 20P configuration for which 4 nodes have been used. The Meso-NH simulations have a very similar computational cost except for STD60 and 20P. For STD60, the more frequent writing and reading of model restart files increases the computational cost by 20%. For 20P, the wall-clock time of the Meso-NH simulation is increased by a factor of 5.6 compared to REF. However, due to using 4 nodes instead of 2, the total cpu time is increased by a factor of 11.2. This is no surprise given the doubling of the number of grid points in all 3 dimensions and the reduction of the time step by a factor of 2. Furthermore, the pressure solver takes more iterations to reach the same precision of the residual for 20P than for REF.

For stardis, the relative differences of wall-clock time and total cpu time between the different configurations are equal since the same number of nodes has been used for all configurations. The computational cost is increased by 33% for DL2 and reduced by 20% for DL8 compared to REF. Given that no deterioration of model results has been found for DL8 compared to REF or DL2, the larger value for the re-injection distance could be used. For MTO300, the computational cost is reduced by 12% compared to REF, which is due to the lower volume of meteorological data that needs to be loaded. Given that the performance for MT0300 is similar to that for REF, the less frequent writing of the meteorological forcing can help to reduce the

https://doi.org/10.5194/egusphere-2026-2061
Preprint. Discussion started: 15 June 2026

Table 1. Computational time for the different configurations.

Configuration	Wall-clock time, Meso-NH [s]	Wall-clock time, stardis [s]	Tot. CPU time, Meso-NH [s]	Tot. CPU time, stardis [s]
REF	6.52×10^5	2.50×10^5	1.67×10^8	3.20×10^8
20P	3.66×10^6	1.45×10^6	1.87×10^9	1.85×10^9
DL2	6.52×10^5	3.33×10^5	1.67×10^8	4.26×10^8
DL8	6.50×10^5	2.01×10^5	1.66×10^8	2.57×10^8
MTO300	6.52×10^5	2.19×10^5	1.67×10^8	2.80×10^8
STD60	7.88×10^5	1.15×10^6	2.02×10^8	1.47×10^9
4REA	6.65×10^5	4.99×10^5	1.70×10^8	6.39×10^8

computational cost. For STD60, the computational cost is increased by a factor of 4.6 compared to REF. This high increase of computational cost is not matched by a relevant improvement of model results. For 4REA, the computational cost is increased by a factor of 2. This is much lower than the increase of the number of realisations (factor of 4), indicating that a lot of time is spent on loading the meteorological forcing data, the building geometry files, and the distribution among processors. 4REA leads to higher precision of T_{surf} for individual probe points, but does not improve the average H or vertical profiles of θ. For 20P, the computational cost increases by a factor of 5.8 compared to REF. This is because the number of probe points increases by a factor of about 4, and a larger volume of meteorological forcing data needs to be read from disc.

The part of the total computational cost required for the calculation of conductive-radiative-convective heat transfer with stardis decreases at higher resolution, since stardis is only employed on the nearly 2-D interface between the city and the atmosphere instead of the 4-D (3 spatial dimensions and time) of the Meso-NH-IBM simulations. For the 10P configuration, stardis accounts for 65% of the total CPU time, whereas for 20P, this has decreased to 50% of the total CPU time. Based on this result it can be expected that the computational time required for stardis will have a smaller percentage for larger simulation domains.

Given the results of the model evaluation (Fig. 8), even larger values of ΔT_{STA} and δ could be tested to further accelerate the simulations.

6 Conclusions

The present study has introduced the coupling between the atmospheric model Meso-NH with Immersed Boundaries to represent builings and the stardis MC solver of conductive-radiative-convective heat exchanges. Meso-NH solves the prognostic equations of the atmospheric variables whereas stardis calculates the surface temperature of urban materials and the ground with a unified MC algorithm taking into account 3-D radiative exchanges in the urban geometry, heat conduction in the build-

https://doi.org/10.5194/egusphere-2026-2061
Preprint. Discussion started: 15 June 2026

ing and ground materials, and convective heat exchange at the surface of the buildings and the ground. This approach to solve conductive-radative-convective heat exchange in a complex urban geometry has become possible thanks to recent breakthroughs in the MC community and is promising to deal with complex geometries, large ranges of scales, and massive parallel computation. The model has been evaluated against experimental data at the impervious outdoor scale model COSMO and it has been shown that the temporal evolution of the sensible heat flux, the vertical profiles of air temperature in the urban roughness sublayer, and the shading patterns on the urban-like obstacles are represented well.

The coupled model is still quite limited since it cannot deal with important processes like water ponds, evaporation or evapotranspiration, air exchange between the building interior and the atmosphere, or heating and air conditioning in buildings. All such processes would be potentially relevant to the simulation of the meteorological impact on humans and infrastructure or to quantify the effectiveness of adaptation measures to climate change. Such processes should be included in future studies. Furthermore, applications to real urban districts and/or the use of grid nesting with lower resolution Meso-NH nests, which do not represent the buildings explicitly, should be explored.

The coupling between Meso-NH and stardis currently relies on writing the required data to disc and running the two models separately. This has a lot of room for improvement, e.g. the data could be kept in memory and the two models executed as one executable. However, another potential option is to use symbolic Monte Carlo that would precompute a large number of radiative paths with stardis in a preprocessing step to Meso-NH and no longer require to excecute stardis during the Meso-NH simulation. This option shall be explored in future work.

Code and data availability. The software archive on Zenodo at https://doi.org/10.5281/zenodo.19497101 (Schoetter et al., 2026) contains the exact model version used in this article and a user manual describing how to install the models and how to run and postprocess the simulations.

Appendix A: Calculation of the exchange coefficient

The exchange coefficient for sensible heat is calculated following the DOE-2 model [2], which allows to differentiate between vertical, upward facing, and downward facing surfaces. Here, first the values for a vertical and a horizontal (upward facing or downward facing) surface are calculated and then weighted as a function of the real surface orientation. In the following formulas, the index for the image point is dropped to improve the readability.

First, the calculation of the exchange coefficient for a vertical surface ($\overline{c_{H,\mathrm{vert}}}$) is given. The exchange coefficient for natural convection ($\overline{c_{H,\mathrm{nat}}}$) is calculated following

$$\overline{c_{H,\mathrm{nat}}} = 1.31 \left|\overline{T} - \overline{T_{\mathrm{surf}}}\right|^{\frac{1}{3}} \tag{A1}$$

[2] https://bigladdersoftware.com/epx/docs/22-2/engineering-reference/outside-surface-heat-balance.html#doe-2-model

https://doi.org/10.5194/egusphere-2026-2061
Preprint. Discussion started: 15 June 2026

The exchange coefficients for a leeward ($\overline{c_{H,\mathrm{lee}}}$) and a windward ($\overline{c_{H,\mathrm{wind}}}$) smooth surface are then calculated following

$$\overline{c_{H,\mathrm{lee}}} = \sqrt{\overline{c_{H,\mathrm{nat}}}^2 + \left(2.86\,\overline{U}^{0.617}\right)^2} \tag{A2}$$

$$\overline{c_{H,\mathrm{wind}}} = \sqrt{\overline{c_{H,\mathrm{nat}}}^2 + \left(2.38\,\overline{U}^{0.89}\right)^2} \tag{A3}$$

with $\overline{U}$ representing the average wind speed at the first layer image points ($\overline{U_{I_1}}$) calculated following

$$\overline{U_{I_1}} = \frac{1}{N_{\mathrm{FRC}}} \sum_{i=0}^{N_{\mathrm{FRC}}-1} \sqrt{u_{I_1}(t - i\,\Delta t_{\mathrm{MNH}})^2 + v_{I_1}(t - i\,\Delta t_{\mathrm{MNH}})^2 + w_{I_1}(t - i\,\Delta t_{\mathrm{MNH}})^2} \tag{A4}$$

Determining whether a surface is located on the windward or leeward side of an obstacle would require non-local calculations and further assumptions which would increase the model complexity. Therefore, a pragmatic average between $\overline{c_{H,\mathrm{lee}}}$ and $\overline{c_{H,\mathrm{wind}}}$ is made to obtain the exchange coefficient for a smooth vertical surface ($\overline{c_{H,\mathrm{smooth}}}$):

$$\overline{c_{H,\mathrm{smooth}}} = 0.5\ (\overline{c_{H,\mathrm{lee}}} + \overline{c_{H,\mathrm{wind}}}) \tag{A5}$$

The exchange coefficient further takes the surface roughness into account for the calculation of $\overline{c_{H,\mathrm{vert}}}$:

$$\overline{c_{H,\mathrm{vert}}} = \overline{c_{H,\mathrm{nat}}} + z_{\mathrm{rough}}(\overline{c_{H,\mathrm{smooth}}} - \overline{c_{H,\mathrm{nat}}}) \tag{A6}$$

where z_{rough} is the surface roughness multiplier. Secondly, the calculation of the exchange coefficient for a horizontal surface ($\overline{c_{H,\mathrm{hor}}}$) is given. For an upward facing surface, $\overline{c_{H,\mathrm{nat}}}$ is calculated following

$$\overline{c_{H,\mathrm{nat}}} = \frac{9.482\,(\overline{T_{\mathrm{surf}}} - \overline{T})^{\frac{1}{3}}}{7.283 - 1} \quad \text{for } \overline{T} < \overline{T_{\mathrm{surf}}} \tag{A7}$$

$$\overline{c_{H,\mathrm{nat}}} = \frac{1.810\,(\overline{T} - \overline{T_{\mathrm{surf}}})^{\frac{1}{3}}}{1.382 + 1} \quad \text{for } \overline{T} \geq \overline{T_{\mathrm{surf}}} \tag{A8}$$

whereas for a downward facing surface it is

$$\overline{c_{H,\mathrm{nat}}} = \frac{9.482\,(\overline{T} - \overline{T_{\mathrm{surf}}})^{\frac{1}{3}}}{7.283 - 1} \quad \text{for } \overline{T} > \overline{T_{\mathrm{surf}}} \tag{A9}$$

$$\overline{c_{H,\mathrm{nat}}} = \frac{1.810\,(\overline{T_{\mathrm{surf}}} - \overline{T})^{\frac{1}{3}}}{1.382 + 1} \quad \text{for } \overline{T} \leq \overline{T_{\mathrm{surf}}} \tag{A10}$$

The exchange coefficient for the smooth horizontal surface is then calculated following

$$\overline{c_{H,\mathrm{smooth}}} = \sqrt{\overline{c_{H,\mathrm{nat}}}^2 + \left(2.86\,\overline{U}^{0.89}\right)^2} \tag{A11}$$

and the exchange coefficient for the horizontal surface is

$$\overline{c_{H,\mathrm{hor}}} = \overline{c_{H,\mathrm{nat}}} + z_{\mathrm{rough}}(\overline{c_{H,\mathrm{smooth}}} - \overline{c_{H,\mathrm{nat}}}) \tag{A12}$$

https://doi.org/10.5194/egusphere-2026-2061
Preprint. Discussion started: 15 June 2026

With the vector from ghost to image $\boldsymbol{GI}(x_I - x_G, y_I - y_G, z_I - z_G)$, the angle ($\beta$) of this vector with respect to the horizontal direction can be calculated following

$$\beta = \arctan\left(\frac{z_I - z_G}{\sqrt{((x_I - x_G)^2 + (y_I - y_G)^2)}}\right) \quad \text{for } \sqrt{((x_I - x_G)^2 + (y_I - y_G)^2)} \neq 0 \tag{A13}$$

$$\beta = -\frac{\pi}{2} \quad \text{for } \sqrt{((x_I - x_G)^2 + (y_I - y_G)^2)} = 0 \text{ and } z_I < z_G \tag{A14}$$

$$\beta = \frac{\pi}{2} \quad \text{for } \sqrt{((x_I - x_G)^2 + (y_I - y_G)^2)} = 0 \text{ and } z_I > z_G \tag{A15}$$

The exchange coefficients for the horizontal and vertical surfaces are then weighted following

$$\overline{c_H} = f_{\text{hor}}\, \overline{c_{H,\text{hor}}} + (1 - f_{\text{hor}})\, \overline{c_{H,\text{vert}}} \tag{A16}$$

with the weighting factor f_{hor} calculated following

$$f_{\text{hor}} = 1 - |\cos(\beta)| \tag{A17}$$

Appendix B: Calculation of the skin surface temperature from the thermal cameras

The skin surface temperature (T_{surf}) is calculated from the observed brightness temperature (T_b) using broadband approximations (Adderley et al. (2015), Morrison et al. (2020)). First, the T_b pixels observed by the camera are converted to broadband longwave radiation flux (LW_{cam}) by Stefan-Boltzmann law

$$LW_{\text{cam}} = \sigma {T_b}^4 \tag{B1}$$

with σ the Stefan-Boltzmann constant (5.67×10^{-8} W m^{-2} K^{-4}). As the COSMO surfaces are non-blackbody (surface emissivity $\epsilon = 0.89$), a portion of the at-sensor radiance is reflected from the sky and ground depending on the facet sky view factor (SVF). The per-facet irradiance contribution from the sky (LW_{sky}) is derived from the upward facing pyrgeometer, (LW) and the SVF:

$$LW_{\text{sky}} = LW\ \nu_{7-14}\ \text{SVF} \tag{B2}$$

with ν_{7-14}, the sky emissivity in the cameras spectral range accounting for differences in pyrgeometer ($\approx$ 4 to 50 µm) and camera (7 to 13 µm) spectral response, taken empirically as $\nu_{7-14} = 0.38$ (Idso, 1981) based on the observed meteorology at COSMO.

The per-facet irradiance contribution from the ground (LW_{ground}) uses the SVF and a per-timestep average of LW_{cam} across all pixels viewing ground surfaces ($\overline{LW_{\text{cam,ground}}}$):

$$LW_{\text{ground}} = (1 - SVF)\ \overline{LW_{\text{cam,ground}}} \tag{B3}$$

Camera pixels are assigned a SVF for each facet type, which is 1 for the cube top, 0.35 for the cube walls, and 0.53 for the ground. Mixed pixels are discarded (Morrison et al., 2018). The broadband surface emission (LW_{surf}) uses the facet irradiance

https://doi.org/10.5194/egusphere-2026-2061
Preprint. Discussion started: 15 June 2026

and the COSMO surface emissivity of $\epsilon = 0.89$:

$$LW_{\mathrm{surf}} = \frac{LW_{\mathrm{cam}} - (1-\epsilon)(LW_{\mathrm{sky}} + LW_{\mathrm{ground}})}{\epsilon} \tag{B4}$$

for calculation of the final T_{surf} by inverse Stefan-Boltzmann law:

$$T_{\mathrm{surf}} = \left(\frac{LW_{\mathrm{surf}}}{\epsilon}\right)^{0.25} \tag{B5}$$

Atmospheric correction is omitted given the short path lengths (<30 m).

Appendix C: Nomenclature

We here provide a nomenclature (Tabs. A1 to A3).

https://doi.org/10.5194/egusphere-2026-2061
Preprint. Discussion started: 15 June 2026

Table A1. Nomenclature

Symbol	Definition	Unit
α	Broadband reflectivity of solar radiation (albedo)	1
c	Volumetric heat capacity	$\mathrm{J\,m^{-3}\,K^{-1}}$
c_H	Turbulent exchange coeffcient for sensible heat	$\mathrm{W\,m^{-2}\,K^{-1}}$
c_m	Specific heat capacity	$\mathrm{J\,kg^{-1}}$
δ_b	Reinjection length used in the stardis conduction algorithm	m
Δ	Resolution of the Meso-NH grid	m
Δt_{FRC}	Time step for writing the Meso-NH forcing data used by stardis	s
Δt_{MNH}	Time step for solving the fluid prognostic equations with Meso-NH	s
Δt_{STA}	Time step for calculation of T_{surf} with stardis	s
ϵ	Broadband emissivity for terrestrial radiation	1
e	Meso-NH prognostic subgrid turbulence kinetic energy	$\mathrm{m^2\,s^{-2}}$
γ_f	Wind direction of forcing	° from North, clockwise
$G(x_G, y_G, z_G)$	Ghost point (position)	m
$\boldsymbol{GI_n}$	Vector from ghost point (G) to nth layer image point (I_n)	m
H	Turbulent sensible heat flux	$\mathrm{W\,m^{-2}}$
H_{mean}	Mean building height of a district	m
i	Loop index	1
$I_n(x_{I,n}, y_{I,n}, z_{I,n})$	Image point of nth layer images (position)	m
κ	von Kármán constant	1
λ	Heat conductivity	$\mathrm{W\,m^{-1}\,K^{-1}}$
λ_p	Plan area building density	1
λ_w	Wall surface density	1
LW	Downwelling terrestrial radiation	$\mathrm{W\,m^{-2}}$

https://doi.org/10.5194/egusphere-2026-2061
Preprint. Discussion started: 15 June 2026

Table A2. Nomenclature, continued

Symbol	Definition	Unit
LW_{cam}	Terrestrial radiation observed by camera	$\mathrm{W\,m^{-2}}$
LW_{ground}	Terrestrial radiation contribution from the ground	$\mathrm{W\,m^{-2}}$
LW_{sky}	Terrestrial radiation contribution from the sky	$\mathrm{W\,m^{-2}}$
ν	Sky emissivity	1
$\boldsymbol{n}$	Vector normal to the solid-fluid interface in Meso-NH-IBM	1
N	Number of MC realisations	1
N_f	Number of facets exchanging radiation	1
N_{FRC}	Number of Meso-NH time steps over which the forcing data are averaged	1
Π	Exner function based on Meso-NH pressure	1
Π_f	Exner function based on forcing pressure	1
p	Pressure simulated by Meso-NH	Pa
ρ_m	Material density	$\mathrm{kg\,m^{-3}}$
σ	Stefan-Boltzmann constant	$\mathrm{W\,m^{-2}\,K^{-4}}$
σ_{Tg}	Average MC standard deviation of ground T_{surf}	K
σ_{Tt}	Average MC standard deviation of cube top T_{surf}	K
σ_{Tw}	Average MC standard deviation of cube wall T_{surf}	K
SW_{dif}	Downwelling diffuse solar radiation	$\mathrm{W\,m^{-2}}$
SW_{dir}	Downwelling direct solar radiation	$\mathrm{W\,m^{-2}}$
t	Simulation time	s
t_k	Simulation time when writing the kth forcing step	s
t_{rel}	Relaxation time constant for nudging in Meso-NH	s
T	Air temperature	K
T_b	Brightness temperature of solid (ground, buildings)	K
T_f	Air temperature of forcing	K
T_{ref}	Reference temperature for infrared radiative exchanges	K
T_{surf}	Skin surface temperature of solid (ground, buildings)	K

https://doi.org/10.5194/egusphere-2026-2061
Preprint. Discussion started: 15 June 2026

Table A3. Nomenclature, continued

Symbol	Definition	Unit
θ	Meso-NH prognostic potential air temperature	K
θ_f	Forcing potential air temperature	K
Φ	Level-set function, $\lvert\Phi\rvert$ is the distance to the solid-fluid interface	m
Ψ	Generic Meso-NH prognostic variable	
Ψ_G	Generic Meso-NH prognostic variable at ghost point (G)	
u	Meso-NH prognostic velocity component in x-direction	$\mathrm{m\,s^{-1}}$
u_f	Forcing velocity component in x-direction	$\mathrm{m\,s^{-1}}$
u_*	Friction velocity	$\mathrm{m\,s^{-1}}$
U_f	Wind speed of forcing	$\mathrm{m\,s^{-1}}$
v	Meso-NH prognostic velocity component in y-direction	$\mathrm{m\,s^{-1}}$
v_f	Forcing velocity component in y-direction	$\mathrm{m\,s^{-1}}$
w	Meso-NH prognostic velocity component in z-direction	$\mathrm{m\,s^{-1}}$
$z_{0,m}$	Bulk momentum roughness length	m
z_{probe}	z-coordinate of probe point	m
z_{rough}	Surface roughness multiplier	1

https://doi.org/10.5194/egusphere-2026-2061
Preprint. Discussion started: 15 June 2026

Author contributions. RS did the Meso-NH and stardis coupling, the execution and analysis of simulations, and the majority of the writing. Cyril Caliot lead the scientific stardis developments required for the calculation of skin surface temperature in the urban environment and develop the stardis library specific to the coupling with Meso-NH. FR, Cyril Caliot, and TN contributed to developed the scripts for the testing and interfacing of the models, and the evaluation of the results with the thermal camera images. Christophe Coustet, VF, and VE performed quality testing, integration, and dissimination of Cyril Caliot's stardis improvements. They furtermore parallelised the probe computation to allow the execution for a large number of probes on a supercomputer. AI provided guidance on the meteorological forcing data, the material parameters, the eddy-covariance, and the thermocouple data from the COSMO site. WM and SK provided guidance on the thermal camera images and the evaluation at the COSMO site. VM supervised the Meso-NH and stardis coupling. FH and NV provided further supervision on the Monte-Carlo modelling. All co-authors have read the entire paper and helped to improve the original draft.

Competing interests. The authors declare no competing interest.

Acknowledgements. Jamie Voogt is acknowleged for discussion on the thermal camera images. This study has been funded by the French Agence Nationale de la Recherche under grant no. ANR-21-CE46-0013 (Monte-Carlo Simulations for Meteorology and Climatology (MC2) project).

https://doi.org/10.5194/egusphere-2026-2061
Preprint. Discussion started: 15 June 2026

References

Adderley, C., Christen, A., and Voogt, J. A.: The effect of radiometer placement and view on inferred directional and hemispheric radiometric temperatures of an urban canopy, Atmospheric Measurement Techniques, 8, 2699–2714, https://doi.org/10.5194/amt-8-2699-2015, 2015.

Akbari, H., Mathews, H. D., and Seto, D.: The long-term effect of increasing the albedo of urban areas, Environmental Research Letters, 7, 024 004, https://doi.org/10.1088/1748-9326/7/2/024004, 2012.

Auguste, F., Réa, G., Paoli, R., Lac, C., Masson, V., and Cariolle, D.: Implementation of an immersed boundary method in the Meso-NH v5.2 model: applications to an idealized urban environment, Geoscientific Model Development, 12, 2607–2633, https://doi.org/10.5194/gmd-12-2607-2019, 2019.

Auguste, F., Lac, C., Masson, V., and Cariolle, D.: Large-Eddy Simulations with an Immersed Boundary Method: Pollutant Dispersion over Urban Terrain, Atmosphere, 11, https://doi.org/10.3390/atmos11010113, 2020.

Biltoft, C. A.: Customer report for Mock Urban Setting Test, Tech. Rep. WDTC-FR-01-121, West Desert Test Center, U.S. Army Dugway Proving Ground, 2001.

Biltoft, C. A., Yee, E., and Jones, C. D.: Overview of the Mock Urban Setting Test (MUST), in: Proceedings of the Fourth Symposium on the Urban Environment. May 20-24, Norfolk, VA., 2002.

Bruse, M. and Fleer, H.: Simulating surface–plant–air interactions inside urban environments with a three dimensional numerical model, Environmental Modelling Software, 13, 373–384, https://doi.org/10.1016/S1364-8152(98)00042-5, 1998.

Bueno, B., Pigeon, G., Norford, L. K., Zibouche, K., and Marchadier, C.: Development and evaluation of a building energy model integrated in the TEB scheme, Geoscientific Model Development, 5, 433–448, https://doi.org/10.5194/gmd-5-433-2012, 2012.

Caliot, C., Schoetter, R., Forest, V., Eymet, V., and Chung, T.-Y.: Model of Spectral and Directional Radiative Transfer in Complex Urban Canopies with Participating Atmospheres, Boundary-Layer Meteorology, 186, 145–175, https://doi.org/10.1007/s10546-022-00750-5, 2023.

Caliot, C., d'Alençon, L., Blanco, S., Forest, V., Fournier, R., Hourdin, F., Retailleau, F., Schoetter, R., and Villefranque, N.: Coupled heat transfers resolution by Monte Carlo in urban geometry including direct and diffuse solar irradiations, International Journal of Heat and Mass Transfer, 222, 125 139, https://doi.org/https://doi.org/10.1016/j.ijheatmasstransfer.2023.125139, 2024.

Caliot, C., d'Alençon, L., Blanco, S., Coustet, C., Eymet, V., Forest, V., Fournier, R., Hourdin, F., Schoetter, R., and Villefranque, N.: Probabilistic Heat Transfer Coupled with Deterministic Flow Simulation for Improved Urban Climate Predictions, in: Proceedings of the 18th International Heat Transfer Conference, 02-07 August 2026, Rio de Janeiro, Brazil, 2026.

Chatterjee, S., Molnár, G., Kiss, B., Topál, D., and Ürge-Vorsatz, D.: Navigating the transition: Modelling the path for net-zero European building sector, Renewable and Sustainable Energy Reviews, 207, 114 827, https://doi.org/https://doi.org/10.1016/j.rser.2024.114827, 2025.

Forceville, G., Lemonsu, A., Goria, S., Stempfelet, M., Host, S., Alessandrini, J.-M., Cordeau, E., and Pascal, M.: Spatial contrasts and temporal changes in fine-scale heat exposure and vulnerability in the Paris region, Science of The Total Environment, 906, 167 476, https://doi.org/https://doi.org/10.1016/j.scitotenv.2023.167476, 2024.

Gabriel, K. M. and Endlicher, W. R.: Urban and rural mortality rates during heat waves in Berlin and Brandenburg, Germany, Environmental Pollution, 159, 2044–2050, https://doi.org/https://doi.org/10.1016/j.envpol.2011.01.016, selected papers from the conference Urban Environmental Pollution: Overcoming Obstacles to Sustainability and Quality of Life (UEP2010), 20-23 June 2010, Boston, USA, 2011.

https://doi.org/10.5194/egusphere-2026-2061
Preprint. Discussion started: 15 June 2026

Gosling, S. N., Lowe, J. A., McGregor, G. R., Pelling, M., and Malamud, B. D.: Associations between elevated atmospheric temperature and human mortality: a critical review of the literature, Climatic Change, 92, 299–341, https://doi.org/10.1007/s10584-008-9441-x, 2009.

Grimmond, C. S. B., Blackett, M., Best, M. J., Barlow, J., Baik, J.-J., Belcher, S. E., Bohnenstengel, S. I., Calmet, I., Chen, F., Dandou, A., Fortuniak, K., Gouvea, M. L., Hamdi, R., Hendry, M., Kawai, T., Kawamoto, Y., Kondo, H., Krayenhoff, E. S., Lee, S.-H., Loridan, T., Martilli, A., Masson, V., Miao, S., Oleson, K., Pigeon, G., Porson, A., Ryu, Y.-H., Salamanca, F., Shashua-Bar, L., Steeneveld, G.-J., Tombrou, M., Voogt, J., Young, D., and Zhang, N.: The International Urban Energy Balance Models Comparison Project: First Results from Phase 1, Journal of Applied Meteorology and Climatology, 49, 1268–1292, https://doi.org/10.1175/2010JAMC2354.1, 2010.

Gunawardena, K., Wells, M., and Kershaw, T.: Utilising green and bluespace to mitigate urban heat island intensity, Science of The Total Environment, 584-585, 1040–1055, https://doi.org/https://doi.org/10.1016/j.scitotenv.2017.01.158, 2017.

Hersbach, H., Bell, B., Berrisford, P., Hirahara, S., Horányi, A., Muñoz-Sabater, J., Nicolas, J., Peubey, C., Radu, R., Schepers, D., Simmons, A., Soci, C., Abdalla, S., Abellan, X., Balsamo, G., Bechtold, P., Biavati, G., Bidlot, J., Bonavita, M., De Chiara, G., Dahlgren, P., Dee, D., Diamantakis, M., Dragani, R., Flemming, J., Forbes, R., Fuentes, M., Geer, A., Haimberger, L., Healy, S., Hogan, R. J., Hólm, E., Janisková, M., Keeley, S., Laloyaux, P., Lopez, P., Lupu, C., Radnoti, G., de Rosnay, P., Rozum, I., Vamborg, F., Villaume, S., and Thépaut, J.-N.: The ERA5 global reanalysis, Quarterly Journal of the Royal Meteorological Society, 146, 1999–2049, https://doi.org/https://doi.org/10.1002/qj.3803, 2020.

Hogan, R. J.: Flexible Treatment of Radiative Transfer in Complex Urban Canopies for Use in Weather and Climate Models, Boundary-Layer Meteorology, 173, 53–78, https://doi.org/10.1007/s10546-019-00457-0, 2019.

Honnert, R., Masson, V., Lac, C., and Nagel, T.: A Theoretical Analysis of Mixing Length for Atmospheric Models From Micro to Large Scales, Frontiers in Earth Science, Volume 8 - 2020, https://doi.org/10.3389/feart.2020.582056, 2021.

Idso, S. B.: A set of equations for full spectrum and 8 to 14 um and 10.5 to 12.5 um thermal radiation from cloudless skies, Water Resources Research, 17, 295–304, https://doi.org/https://doi.org/10.1029/WR017i002p00295, 1981.

Inagaki, A. and Kanda, M.: Turbulent flow similarity over an array of cubes in near-neutrally stratified atmospheric flow, Journal of Fluid Mechanics, 615, 101–120, https://doi.org/10.1017/S0022112008003765, 2008.

Inagaki, A. and Kanda, M.: Organized Structure of Active Turbulence Over an Array of Cubes within the Logarithmic Layer of Atmospheric Flow, Boundary-Layer Meteorology, 135, 209–228, https://doi.org/10.1007/s10546-010-9477-0, 2010.

IPCC: Climate Change 2022: Impacts, Adaptation and Vulnerability, Summary for Policymakers, Cambridge University Press, Cambridge, UK and New York, USA, ISBN 9781009325844, 2022.

Kanda, M., Kawai, T., Kanega, M., Moriwaki, R., Narita, K., and Hagishima, A.: A Simple Energy Balance Model for Regular Building Arrays, Boundary-Layer Meteorology, 116, 423–443, https://doi.org/10.1007/s10546-004-7956-x, 2005.

Kanda, M., Kanega, M., Kawai, T., Moriwaki, R., and Sugawara, H.: Roughness Lengths for Momentum and Heat Derived from Outdoor Urban Scale Models, Journal of Applied Meteorology and Climatology, 46, 1067–1079, https://doi.org/10.1175/JAM2500.1, 2007.

Kawai, T. and Kanda, M.: Urban Energy Balance Obtained from the Comprehensive Outdoor Scale Model Experiment. Part I: Basic Features of the Surface Energy Balance, Journal of Applied Meteorology and Climatology, 49, 1341–1359, https://doi.org/10.1175/2010JAMC1992.1, 2010.

Kawai, T., Kanda, M., Narita, K., and Hagishima, A.: Validation of a numerical model for urban energy-exchange using outdoor scale-model measurements, International Journal of Climatology, 27, 1931–1942, https://doi.org/https://doi.org/10.1002/joc.1624, 2007.

https://doi.org/10.5194/egusphere-2026-2061
Preprint. Discussion started: 15 June 2026

Kikegawa, Y., Genchi, Y., Yoshikado, H., and Kondo, H.: Development of a numerical simulation system toward comprehensive assessments of urban warming countermeasures including their impacts upon the urban buildings' energy-demands, Applied Energy, 76, 449–466, https://doi.org/10.1016/S0306-2619(03)00009-6, 2003.

Krayenhoff, E. S., Christen, A., Martilli, A., and Oke, T. R.: A Multi-layer Radiation Model for Urban Neighbourhoods with Trees, Boundary-Layer Meteorology, 151, 139–178, https://doi.org/10.1007/s10546-013-9883-1, 2014.

Krč, P., Resler, J., Sühring, M., Schubert, S., Salim, M. H., and Fuka, V.: Radiative Transfer Model 3.0 integrated into the PALM model system 6.0, Geoscientific Model Development, 14, 3095–3120, https://doi.org/10.5194/gmd-14-3095-2021, 2021.

Kusaka, H., Kondo, H., Kikegawa, Y., and Kimura, F.: A Simple Single-Layer Urban Canopy Model For Atmospheric Models: Comparison With Multi-Layer And Slab Models, Boundary-Layer Meteorology, 101, 329–358, https://doi.org/10.1023/A:1019207923078, 2001.

Kusaka, H., Ikeda, R., Sato, T., Iizuka, S., and Boku, T.: Development of a Multi-Scale Meteorological Large-Eddy Simulation Model for Urban Thermal Environmental Studies: The "City-LES" Model Version 2.0, Journal of Advances in Modeling Earth Systems, 16, e2024MS004 367, https://doi.org/https://doi.org/10.1029/2024MS004367, e2024MS004367 2024MS004367, 2024.

Lac, C., Chaboureau, J.-P., Masson, V., Pinty, J.-P., Tulet, P., Escobar, J., Leriche, M., Barthe, C., Aouizerats, B., Augros, C., Aumond, P., Auguste, F., Bechtold, P., Berthet, S., Bielli, S., Bosseur, F., Caumont, O., Cohard, J.-M., Colin, J., Couvreux, F., Cuxart, J., Delautier, G., Dauhut, T., Ducrocq, V., Filippi, J.-B., Gazen, D., Geoffroy, O., Gheusi, F., Honnert, R., Lafore, J.-P., Lebeaupin Brossier, C., Libois, Q., Lunet, T., Mari, C., Maric, T., Mascart, P., Mogé, M., Molinié, G., Nuissier, O., Pantillon, F., Peyrillé, P., Pergaud, J., Perraud, E., Pianezze, J., Redelsperger, J.-L., Ricard, D., Richard, E., Riette, S., Rodier, Q., Schoetter, R., Seyfried, L., Stein, J., Suhre, K., Taufour, M., Thouron, O., Turner, S., Verrelle, A., Vié, B., Visentin, F., Vionnet, V., and Wautelet, P.: Overview of the Meso-NH model version 5.4 and its applications, Geoscientific Model Development, 11, 1929–1969, https://doi.org/10.5194/gmd-11-1929-2018, 2018.

Lemonsu, A. and Masson, V.: Simulation of a Summer Urban Breeze Over Paris, Boundary-Layer Meteorology, 104, 463–490, https://doi.org/10.1023/A:1016509614936, 2002.

Lemonsu, A., Caillaud, C., Alias, A., Riette, S., Seity, Y., Le Roy, B., Michau, Y., and Lucas-Picher, P.: What added value of CNRM-AROME convection-permitting regional climate model compared to CNRM-ALADIN regional climate model for urban climate studies? Evaluation over Paris area (France), Climate Dynamics, 61, 1643–1661, https://doi.org/10.1007/s00382-022-06647-w, 2023.

Li, X., Zhou, Y., Yu, S., Jia, G., Li, H., and Li, W.: Urban heat island impacts on building energy consumption: A review of approaches and findings, Energy, 174, 407–419, https://doi.org/https://doi.org/10.1016/j.energy.2019.02.183, 2019.

Lipson, M. J., Grimmond, S., Best, M., Abramowitz, G., Coutts, A., Tapper, N., Baik, J.-J., Beyers, M., Blunn, L., Boussetta, S., Bou-Zeid, E., De Kauwe, M. G., de Munck, C., Demuzere, M., Fatichi, S., Fortuniak, K., Han, B.-S., Hendry, M. A., Kikegawa, Y., Kondo, H., Lee, D.-I., Lee, S.-H., Lemonsu, A., Machado, T., Manoli, G., Martilli, A., Masson, V., McNorton, J., Meili, N., Meyer, D., Nice, K. A., Oleson, K. W., Park, S.-B., Roth, M., Schoetter, R., Simón-Moral, A., Steeneveld, G.-J., Sun, T., Takane, Y., Thatcher, M., Tsiringakis, A., Varentsov, M., Wang, C., Wang, Z.-H., and Pitman, A. J.: Evaluation of 30 urban land surface models in the Urban-PLUMBER project: Phase 1 results, Quarterly Journal of the Royal Meteorological Society, 150, 126–169, https://doi.org/https://doi.org/10.1002/qj.4589, 2024.

Lundquist, K. A., Chow, F. K., and Lundquist, J. K.: An Immersed Boundary Method Enabling Large-Eddy Simulations of Flow over Complex Terrain in the WRF Model, Monthly Weather Review, 140, 3936–3955, https://doi.org/10.1175/MWR-D-11-00311.1, 2012.

Lunet, T., Lac, C., Auguste, F., Visentin, F., Masson, V., and Escobar, J.: Combination of WENO and Explicit Runge–Kutta Methods for Wind Transport in the Meso-NH Model, Monthly Weather Review, 145, 3817–3838, https://doi.org/10.1175/MWR-D-16-0343.1, 2017.

https://doi.org/10.5194/egusphere-2026-2061
Preprint. Discussion started: 15 June 2026

Maronga, B., Banzhaf, S., Burmeister, C., Esch, T., Forkel, R., Fröhlich, D., Fuka, V., Gehrke, K. F., Geletič, J., Giersch, S., Gronemeier, T., Groß, G., Heldens, W., Hellsten, A., Hoffmann, F., Inagaki, A., Kadasch, E., Kanani-Sühring, F., Ketelsen, K., Khan, B. A., Knigge, C., Knoop, H., Krč, P., Kurppa, M., Maamari, H., Matzarakis, A., Mauder, M., Pallasch, M., Pavlik, D., Pfafferott, J., Resler, J., Rissmann, S., Russo, E., Salim, M., Schrempf, M., Schwenkel, J., Seckmeyer, G., Schubert, S., Sühring, M., von Tils, R., Vollmer, L., Ward, S., Witha, B., Wurps, H., Zeidler, J., and Raasch, S.: Overview of the PALM model system 6.0, Geoscientific Model Development, 13, 1335–1372, https://doi.org/10.5194/gmd-13-1335-2020, 2020.

Martilli, A., Clappier, A., and Rotach, M. W.: An Urban Surface Exchange Parameterisation for Mesoscale Models, Boundary-Layer Meteorology, 104, 261–304, https://doi.org/10.1023/A:1016099921195, 2002.

Masson, V.: A Physically-Based Scheme For The Urban Energy Budget In Atmospheric Models, Boundary-Layer Meteorology, 94, 357–397, https://doi.org/10.1023/A:1002463829265, 2000.

Masson, V., Bonhomme, M., Salagnac, J.-L., Briottet, X., and Lemonsu, A.: Solar panels reduce both global warming and urban heat island, Frontiers in Environmental Science, 2, 1–10, 2014.

Masson, V., Lemonsu, A., Hidalgo, J., and Voogt, J.: Urban Climates and Climate Change, Annual Review of Environment and Resources, 45, 411–444, https://doi.org/https://doi.org/10.1146/annurev-environ-012320-083623, 2020.

Moonen, P., Defraeye, T., Dorer, V., Blocken, B., and Carmeliet, J.: Urban physics: effect of the micro-climate on comfort, health and energy demand, Frontiers in Architectural Research, 1, 197–228, https://doi.org/10.1016/j.foar.2012.05.002, 2012.

Morille, B., Lauzet, N., and Musy, M.: SOLENE-microclimate: A Tool to Evaluate Envelopes Efficiency on Energy Consumption at District Scale., Energy Procedia, 78, 1165–1170, https://doi.org/https://doi.org/10.1016/j.egypro.2015.11.088, 6th International Building Physics Conference, IBPC 2015, 2015.

Morrison, W., Kotthaus, S., Grimmond, C., Inagaki, A., Yin, T., Gastellu-Etchegorry, J.-P., Kanda, M., and Merchant, C. J.: A novel method to obtain three-dimensional urban surface temperature from ground-based thermography, Remote Sensing of Environment, 215, 268–283, https://doi.org/10.1016/j.rse.2018.05.004, 2018.

Morrison, W., Yin, T., Lauret, N., Guilleux, J., Kotthaus, S., Gastellu-Etchegorry, J.-P., Norford, L., and Grimmond, S.: Atmospheric and emissivity corrections for ground-based thermography using 3D radiative transfer modelling, Remote Sensing of Environment, 237, 111 524, https://doi.org/10.1016/j.rse.2019.111524, 2020.

Muñoz-Esparza, D., Sauer, J. A., Shin, H. H., Sharman, R., Kosović, B., Meech, S., García-Sánchez, C., Steiner, M., Knievel, J., Pinto, J., and Swerdlin, S.: Inclusion of Building-Resolving Capabilities Into the FastEddy® GPU-LES Model Using an Immersed Body Force Method, Journal of Advances in Modeling Earth Systems, 12, e2020MS002 141, https://doi.org/https://doi.org/10.1029/2020MS002141, e2020MS002141 10.1029/2020MS002141, 2020.

Nagel, T., Schoetter, R., Masson, V., Lac, C., and Carissimo, B.: Numerical Analysis of the Atmospheric Boundary-Layer Turbulence Influence on Microscale Transport of Pollutant in an Idealized Urban Environment, Boundary-Layer Meteorology, 184, 113–141, https://doi.org/10.1007/s10546-022-00697-7, 2022.

Nagel, T., Schoetter, R., Bourgin, V., Masson, V., and Onofri, E.: Drag Coefficient and Turbulence Mixing Length of Local Climate Zone-Based Urban Morphologies Derived Using Obstacle-Resolving Modelling, Boundary-Layer Meteorology, 186, 737–769, https://doi.org/10.1007/s10546-022-00780-z, 2023.

Norton, B. A., Coutts, A. M., Livesley, S. J., Harris, R. J., Hunter, A. M., and Williams, N. S.: Planning for cooler cities: A framework to prioritise green infrastructure to mitigate high temperatures in urban landscapes, Landscape and Urban Planning, 134, 127–138, https://doi.org/https://doi.org/10.1016/j.landurbplan.2014.10.018, 2015.

https://doi.org/10.5194/egusphere-2026-2061
Preprint. Discussion started: 15 June 2026

Oke, T.: City size and the urban heat island, Atmospheric Environment (1967), 7, 769–779, https://doi.org/https://doi.org/10.1016/0004-6981(73)90140-6, 1973.

Oke, T. R., Mills, G., Christen, A., and Voogt, J. A.: Urban Climates, Cambridge University Press, https://doi.org/10.1017/9781139016476, 2017.

Pfafferott, J., Rißmann, S., Sühring, M., Kanani-Sühring, F., and Maronga, B.: Building indoor model in PALM-4U: indoor climate, energy demand, and the interaction between buildings and the urban microclimate, Geoscientific Model Development, 14, 3511–3519, https://doi.org/10.5194/gmd-14-3511-2021, 2021.

Salamanca, F., Krpo, A., Martilli, A., and Clappier, A.: A new building energy model coupled with an urban canopy parameterization for urban climate simulations—part I. formulation, verification, and sensitivity analysis of the model, Theoretical and Applied Climatology, 99, 331, https://doi.org/10.1007/s00704-009-0142-9, 2009.

Schoetter, R., Caliot, C., Chung, T.-Y., Hogan, R. J., and Masson, V.: Quantification of Uncertainties of Radiative Transfer Calculation in Urban Canopy Models, Boundary-Layer Meteorology, https://doi.org/https://doi.org/10.1007/s10546-023-00827-9, 2023.

Schoetter, R., Cyril, C., Retailleau, F., Nagel, T., Coustet, C., Eymet, V., Forest, V., Hourdin, F., Inagaki, A., Kotthaus, S., Masson, V., Morrison, W., and Villefranque, N.: Source code, numerical simulations, and post processing scripts described in the research article "Coupling the atmospheric model Meso- NH-v5.5 with the Monte-Carlo solver of conductive- radiative-convective heat exchanges stardis-v0.11.1 to calculate the surface energy balance of complex geometries", submitted to Geoscientific Model Development, https://doi.org/10.5281/zenodo.19497101, 2026.

Seity, Y., Brousseau, P., Malardel, S., Hello, G., Bénard, P., Bouttier, F., Lac, C., and Masson, V.: The AROME-France Convective-Scale Operational Model, Monthly Weather Review, 139, 976–991, https://doi.org/10.1175/2010MWR3425.1, 2011.

Suter, I., Grylls, T., Sützl, B. S., Owens, S. O., Wilson, C. E., and van Reeuwijk, M.: uDALES 1.0: a large-eddy simulation model for urban environments, Geoscientific Model Development, 15, 5309–5335, https://doi.org/10.5194/gmd-15-5309-2022, 2022.

Toparlar, Y., Blocken, B., Maiheu, B., and van Heijst, G.: A review on the CFD analysis of urban microclimate, Renewable and Sustainable Energy Reviews, 80, 1613–1640, https://doi.org/https://doi.org/10.1016/j.rser.2017.05.248, 2017.

Tregan, J. M., Amestoy, J. L., Bati, M., Bezian, J.-J., Blanco, S., Brunel, L., Caliot, C., Charon, J., Cornet, J.-F., Coustet, C., d'Alençon, L., Dauchet, J., Dutour, S., Eibner, S., El Hafi, M., Eymet, V., Farges, O., Forest, V., Fournier, R., Galtier, M., Gattepaille, V., Gautrais, J., He, Z., Hourdin, F., Ibarrart, L., Joly, J.-L., Lapeyre, P., Lavieille, P., Lecureux, M.-H., Lluc, J., Miscevic, M., Mourtaday, N., Nyffenegger-Péré, Y., Pelissier, L., Penazzi, L., Piaud, B., Rodrigues-Viguier, C., Roques, G., Roger, M., Saez, T., Terrée, G., Villefranque, N., Vourc'h, T., and Yaacoub, D.: Coupling radiative, conductive and convective heat-transfers in a single Monte Carlo algorithm: A general theoretical framework for linear situations, PLOS ONE, 18, 1–54, https://doi.org/10.1371/journal.pone.0283681, 2023.

Villefranque, N., Hourdin, F., d'Alençon, L., Blanco, S., Boucher, O., Caliot, C., Coustet, C., Dauchet, J., Hafi, M. E., Eymet, V., Farges, O., Forest, V., Fournier, R., Gautrais, J., Masson, V., Piaud, B., and Schoetter, R.: The "teapot in a city": A paradigm shift in urban climate modeling, Science Advances, 8, eabp8934, https://doi.org/10.1126/sciadv.abp8934, 2022.

Yang, X. and Li, Y.: Development of a Three-Dimensional Urban Energy Model for Predicting and Understanding Surface Temperature Distribution, Boundary-Layer Meteorology, 149, 303–321, https://doi.org/10.1007/s10546-013-9842-x, 2013.